JACS
JOURNAL OF THE AMERICAN CHEMICAL SOCIETY
pubs.acs.org/JACS
Article

Theory and Applications of Nitroxide-based Paramagnetic Cosolutes for Probing Intermolecular and Electrostatic Interactions on Protein Surfaces

Yusuke Okuno, Charles D. Schwieters, Zhilin Yang, and G. Marius Clore*

Cite This: J. Am. Chem. Soc. 2022, 144, 21371−21388
Read Online
ACCESS | Metrics & More | Article Recommendations | Supporting Information

ABSTRACT: Solvent paramagnetic relaxation enhancement (sPRE) arising from nitroxide-based cosolutes has recently been used to provide an atomic view of cosolute-induced protein denaturation and to characterize residue-specific effective near-surface electrostatic potentials (ϕ_{ENS}). Here, we explore distinct properties of the sPRE arising from nitroxide-based cosolutes and provide new insights into the interpretation of the sPRE and sPRE-derived ϕ_{ENS}. We show that: (a) the longitudinal sPRE rate Γ_1 is heavily dependent on spectrometer field and viscosity, while the transverse sPRE rate Γ_2 is much less so; (b) the spectral density $J(0)$ is proportional to the inverse of the relative translational diffusion constant and is related to the quantity $\langle r^{-4}\rangle_{norm}$, a concentration-normalized equilibrium average of the electron−proton interspin separation; and (c) attractive intermolecular interactions result in a shortening of the residue-specific effective correlation time for the electron−proton vector. We discuss four different approaches for evaluating ϕ_{ENS} based on Γ_2, $J(0)$, Γ_1, or $\langle r^{-6}\rangle_{norm}$. The latter is evaluated from the magnetic field dependence of Γ_1 in conjunction with Γ_2. Long-range interactions dominate $J(0)$ and Γ_2, while, at high magnetic fields, the contribution of short-range interactions becomes significant for $J(\omega)$ and hence Γ_1; the four ϕ_{ENS} quantities enable one to probe both long- and short-range electrostatic interactions. The experimental ϕ_{ENS} potentials were evaluated using three model protein systems, two folded (ubiquitin and native drkN SH3) and one intrinsically disordered (unfolded state of drkN SH3), in relation to theoretical ϕ_{ENS} potentials calculated from atomic coordinates using the Poisson-Boltzmann theory with either a r^{-6} or r^{-4} dependence.

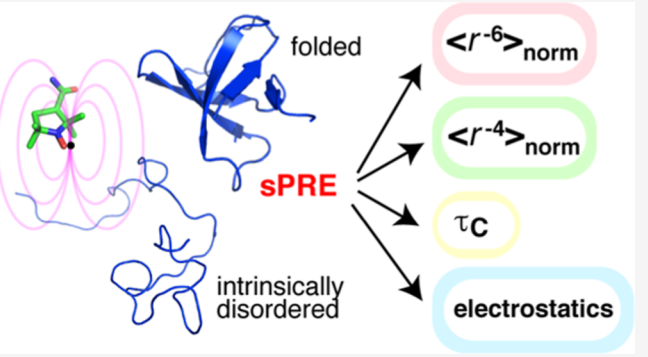

INTRODUCTION

Solvent paramagnetic relaxation enhancement (sPRE) has been used to study protein solvent accessibility,[1−16] to refine NMR protein structures,[17−19] to investigate protein−cosolute interactions,[20,21] and to characterize the electrostatic potential of small molecules and proteins.[22−29] The paramagnetic moiety of the cosolutes employed in these studies comprises either a paramagnetic metal ion or a nitroxide free radical. Paramagnetic metal ions have also been used as contrast reagents in magnetic resonance imaging (MRI), and the development of theoretical and experimental methods for the analysis of the sPRE in the context of MRI has been the subject of extensive investigation.[30−34] Although nitroxide free radicals, such as hydroxy-TEMPO (4-hydroxy-2,2,6,6-tetramethylpiperidin-1-oxyl), have been widely used in the past to study protein solvent accessibility,[1−11] their intrinsic hydrophobicity makes quantitative interpretation difficult, as they tend to bind preferentially to hydrophobic regions on the protein surface. For this reason, less hydrophobic, chelated metal ion complexes, such as gadolinium-diethylenetriamine pentaacetic acid-bismethylamide, are better suited for characterizing protein solvent exposure and for protein structure refinement.[12,19,35] Recently, nitroxide-based paramagnetic solutes have been employed as polarizing agents in liquid state dynamic nuclear polarization.[36−39]

Previously, we showed that nitroxide-based cosolutes can be used to provide quantitative measures of the energetics and dynamics of cosolute−protein interactions at atomic resolution through two parameters obtained by simultaneously fitting the transverse sPRE (Γ_2) at one spectrometer field and the longitudinal sPRE (Γ_1) at multiple spectrometer fields to an ansatz spectral density function comprising a concentration-normalized equilibrium average of the interspin separation, $\langle r^{-6}\rangle_{norm}$, and an effective correlation time τ_C for the electron−proton vector.[20] Using this approach, we were able to probe

Received: September 20, 2022
Published: November 8, 2022

https://doi.org/10.1021/jacs.2c10035
J. Am. Chem. Soc. 2022, 144, 21371−21388

the mechanism of nitroxide cosolute-induced protein denaturation for a model protein drkN SH3 that exists as an equilibrium mixture of native folded and unfolded states.[21] Extending this work, Yu et al.[28] recently proposed an approach to characterize the effective near-surface electrostatic potential (ϕ_{ENS}) of proteins by measuring the transverse sPRE for two different nitroxide-based paramagnetic cosolutes of opposite charge. Very recently, this approach has been used to map the residue-specific ϕ_{ENS} potential for the intrinsically disordered region of the protein CAPRIN1 along its phase-separation trajectory.[40]

In this paper, we present a theoretical analysis of the intrinsic properties of the sPRE arising from nitroxide-based paramagnetic cosolutes and present a new interpretation of transverse sPRE rates (Γ_2) through a concentration-normalized equilibrium-averaged interspin distance $\langle r^{-4}\rangle_{norm}$. We analyze four different experimentally accessible measures of the residue-specific effective near-surface eletrostatic potential calculated from Γ_2, $J(0)$, Γ_1, or $\langle r^{-6}\rangle_{norm}$, each of which exhibits different distance dependencies, thereby enabling one to discriminate between long- and short-range electrostatic interactions. The four different residue-specific ϕ_{ENS} quantities were determined experimentally for three protein model systems, two folded (ubiquitin and native drkN SH3) and one intrinsically disordered (the unfolded state of drkN SH3), and evaluated against the theoretical ϕ^{PB}_{ENS} values calculated from molecular coordinates using Poisson-Boltzmann theory with either an r^{-6} or r^{-4} distance dependence.

The outline of the paper is as follows. We first review the general theory of the sPRE and obtain an expression of the sPRE in terms of the spectral densities. We then discuss the impact of different relaxation mechanisms for paramagnetic metal ions and nitroxide-based paramagnetic cosolutes. Subsequent discussion pertains to limitations and current progress in the analysis of the sPRE arising from nitroxide-based cosolutes. In the Result and Discussion section, we provide new insights into the interpretation of sPRE rates and ϕ_{ENS}. First, the distinct properties of the transverse (Γ_2) and longitudinal (Γ_1) sPRE relaxation rates are discussed, and new approaches for directly interpreting these relaxation rates are proposed. We then provide a theoretical basis for the physical interpretation of the effective correlation time τ_C. We show that for outer-sphere relaxation, originating from nitroxide-based cosolutes, attractive interactions counterintuitively result in shorter τ_C values, which is the opposite of the expected result for inner- or second-sphere relaxation, where the cosolute and protein form weak rotational-coupled complexes. We then turn to the study of protein electrostatics using the sPRE and introduce different approaches and interpretations to understand the nature of the ϕ_{ENS} potential derived from experimental sPRE measurements. Finally, we analyze the effects of short-range interactions involving different locations on the cosolute relative to the position of the unpaired electron.

BASIC THEORETICAL CONSIDERATIONS

We first lay out the basic theory related to the sPRE that is required to understand the new derivations related to the properties of the longitudinal (Γ_1) and transverse (Γ_2) sPRE rates and their application to the study of protein electrostatics presented in the Results and Discussion section.

General Expressions for Longitudinal (Γ_1) and Transverse (Γ_2) Paramagnetic Relaxation Enhancement in Terms of Spectral Densities. The dipole−dipole correlation function in an isotropic liquid is given by[41,42]

$$C(t) = N_S\left\langle \frac{P_2(\hat{r}(t)\cdot\hat{r}_o)}{r^3(t)r_o^3}\right\rangle \tag{1}$$

where r and $\hat{r}$ are the length and orientation of the interspin vector $\vec{r}$; $P_2(x)$ is the Legendre polynomial of degree 2; and N_S is the number of paramagnetic cosolute molecules in the system. The subscript "o" denotes the quantity at $t = 0$. The spectral density $J(\omega)$ is given by the cosine transform of $C(t)$

$$J(\omega) = \int_0^\infty C(t)\cos(\omega t)\mathrm{d}t \tag{2}$$

where ω is the angular frequency in radians.s^{-1} and is related to the spectrometer frequency (ν) in Hz by $\omega = 2\pi\nu$.

Equation 2 ignores the contribution of electron spin relaxation. For the simplest model where the electron spin S is assumed to relax as a single exponential with rates $1/T_{1e}$ and $1/T_{2e}$ for longitudinal and transverse relaxation, respectively, eq 2 is modified to[31]

$$J(\omega, T_{ie}) = \mathrm{Re}\int_0^\infty C(t)\exp(-(i\omega + T_{ie}^{-1})t)\mathrm{d}t \tag{3}$$

where i = 1 or 2. In the absence of electron relaxation, eq 3 reduces to eq 2.

The longitudinal (Γ_1) and transverse (Γ_2) sPREs are defined as the difference in the longitudinal and transverse relaxation rates, respectively, of a protein nuclear spin (generally a proton) in the presence and absence of the paramagnetic cosolute.[43] Γ_1 and Γ_2 are related to the spectral density function $J(\omega,T_{ie})$ by[44−46]

$$\begin{aligned}\Gamma_1 = \left(\frac{\mu_o}{4\pi}\right)^2\hbar^2\gamma_H^2\gamma_e^2\frac{2}{15}[S(S+1)\{&J(\omega_H-\omega_e, T_{2e})\\ &+ 3J(\omega_H, T_{1e}) + 6J(\omega_H+\omega_e, T_{2e})\}\\ &+ 9\langle S_z\rangle^2\{J(\omega_H, 0) - J(\omega_H, T_{1e})\}]\end{aligned} \tag{4}$$

$$\begin{aligned}\Gamma_2 = \left(\frac{\mu_o}{4\pi}\right)^2\hbar^2\gamma_H^2\gamma_e^2\frac{1}{15}[S(S+1)\{&(J(\omega_H-\omega_e, T_{2e})\\ &+ 3J(\omega_H, T_{1e}) + 4J(0, T_{1e}) + 6J(\omega_e, T_{2e})\\ &+ 6J(\omega_H+\omega_e, T_{2e}))\} + \langle S_z\rangle^2\{12(J(0,0) - J(0, T_{1e}))\\ &+ 9(J(\omega_H, 0) - J(\omega_H, T_{1e}))\}]\end{aligned} \tag{5}$$

where γ_H and γ_e are the gyromagnetic ratios of the proton and electron, respectively; μ_o is the vacuum permittivity constant; $\hbar$ is Planck's constant divided by 2π; ω_H is the angular frequency of the proton; B_o is the external magnetic field; k_B is the Boltzmann constant; and T is temperature. The thermal average of the z component of spin S (denoted as S_z), in the high temperature limit, is given by

$$\begin{aligned}\langle S_z\rangle &= \frac{\sum_{m=-S}^{S} m\exp\left(m\frac{\hbar\gamma_e B_o}{k_B T}\right)}{\sum_{m=-S}^{S}\exp\left(m\frac{\hbar\gamma_e B_o}{k_B T}\right)}\\ &\approx \frac{1}{2S+1}\left(\frac{\hbar\gamma_e B_o}{k_B T}\right)\sum_{m=-S}^{S} m^2 = \frac{S(S+1)}{3}\left(\frac{\hbar\gamma_e B_o}{k_B T}\right)\end{aligned} \tag{6}$$

https://doi.org/10.1021/jacs.2c10035
J. Am. Chem. Soc. 2022, 144, 21371−21388

In both eqs 4 and 5 there is a term proportional to $\langle S_z \rangle^2$, which corresponds to the contribution from Curie relaxation.[45] From eq 6, the contribution from Curie relaxation scales with the magnetic field, but $\langle S_z \rangle$ remains small even at high field (e.g., 0.024 at a ^{1}H Larmor frequency of 900 MHz at 298 K for $S = 1/2$). Further, if the longitudinal relaxation time of the electron, T_{1e}, is much longer than the decay timescale of $C(t)$ (usually in the low nanosecond time-range), $J(\omega, 0) \approx J(\omega, T_{1e})$, and the contribution from Curie relaxation becomes negligibly small. This is especially true for nitroxide-based paramagnetic cosolutes, as T_{1e} ranges from 100 ns to microseconds.[47−49] Lanthanide-based paramagnetic metal ions, such as Tb^{3+} and Yb^{3+}, have very fast electronic relaxation, $T_{1e} < 1$ ps,[50] so that $J(\omega, 0) \gg J(\omega, T_{1e})$, and Curie relaxation contributes significantly to the overall relaxation process.

In the current work, we are only concerned with nitroxide-based paramagnetic cosolutes with $S = 1/2$, where $J(\omega) = J(\omega, 0) \approx J(\omega, T_{1e})$, and Curie relaxation can be neglected. Further, the sPRE experiments are performed at high field so that $J(\omega_H) \gg J(\omega_e)$, and all the terms involving ω_e can be neglected. Under such conditions, eqs 4 and 5 reduce to the usual expressions[43] given by

$$\Gamma_1 = \frac{3}{10}\left(\frac{\mu_0}{4\pi}\right)^2 \hbar^2 \gamma_H^2 \gamma_e^2 J(\omega_H) \tag{7}$$

and

$$\Gamma_2 = \frac{1}{5}\left(\frac{\mu_0}{4\pi}\right)^2 \hbar^2 \gamma_H^2 \gamma_e^2 \left(J(0) + \frac{3}{4} J(\omega_H)\right) \tag{8}$$

From eqs 7 and 8, it follows that the experimentally observable sPREs arising from nitroxide-based cosolutes, are completely determined by the points on the spectral densities. Consequently, what we may expect to learn from the sPRE experiments is contained in the details of the spectral densities.

Relaxation Mechanisms of Paramagnetic Metal Ion and Nitroxide-based Paramagnetic Cosolutes. Three different relaxation mechanisms have been used to describe the sPRE arising from paramagnetic metal ions: inner-, second-, and outer-sphere relaxation.[33,37,51] Inner-sphere relaxation is usually used to describe the case where the proton(s) of interest forms a defined coordination with the paramagnetic metal ion; an example would be a water molecule in the first-coordination sphere of the paramagnetic metal ion. The interspin distance between the proton and paramagnetic metal ion is assumed to be fixed, and the spectral densities are described by the Solomon-Bloembergen (SB) equation.[52,53] Second-sphere relaxation occurs when the proton forms a hydrogen bond with ligands in the paramagnetic metal ion complex.[32,33] The interspin distance is also assumed to be fixed, and the spectral densities can be modeled by the SB equation. Lastly, the outer-sphere relaxation mechanism arises from translational diffusion of the paramagnetic cosolute and the molecule of interest and, consequently, the interspin distance is not fixed and varies with time. The spectral densities for outer-sphere relaxation are usually modeled using a center-spin force-free hard-sphere model (denoted as FFHS) developed by Hwang and Freed[54] and Ayant et al.[55] (see eq S3.9). Further details relating to these three relaxation mechanisms can be found in refs 32−34.

In this paper, we focus on nitroxide-based paramagnetic cosolutes, and the definition of inner- and second-sphere relaxation mechanisms is not directly applicable, as nitroxide-based paramagnetic cosolutes are not equivalent to metal ions or metal-ion complexes. Here, we follow the definitions given in the literature[37,38,56] and collectively refer to inner-sphere relaxation as any relaxation mechanism resulting from the formation of a well-defined complex between the paramagnetic cosolute and a protein with a well-defined interspin distance. Outer-sphere relaxation for nitroxide-based paramagnetic cosolutes is defined in the same way as that for paramagnetic metal ions discussed above (see Figure S1).

Neugebauer et al.[38] carried out extensive ^{1}H relaxivity nuclear magnetic relaxation dispersion (NMRD) measurements on DMSO, toluene, and acetone in the presence of TEMPOL (4-hydroxy-2,2,6,6-tetramethylpiperidine-1-oxy) over Larmor frequencies ranging from 0.01 to 950 MHz, complemented by the measurement of dynamic nuclear polarization coupling factors over temperatures ranging from 25 to 80 °C. The NMRD profiles cannot be fit with the Solomon-Bloembergen spectral densities that describe inner-sphere relaxation (see Figure S8 of ref 20 and Figure 5 of ref 56). In the second section of the Supporting Information, we present a detailed discussion and analysis of the NMRD and DNP coupling factor data. We show that the NMRD data at all temperatures can be fully accounted for by the idealized center-spin FFHS model that describes outer-sphere relaxation (Supporting Information Figure S2). For acetone, the center-spin FFHS model using the parameters obtained from the fits to the NMRD data from 25 to 80 °C is sufficient to account for the temperature dependence of the DNP data; for DMSO and toluene, however, the NMRD data have to be fit to an off-center spin FFHS model (which is also physically more realistic) to correctly back-calculate the DNP data (Figure S2). The NMRD data for DMSO and toluene can also be fit using a linear combination of inner- and outer-sphere relaxation, which also results in good prediction of the DNP coupling factors (Figures S3 and S4, and Table S3). The maximum contribution of inner-sphere relaxation to $J(0)$, however, is negligibly small (less than ∼5%; see Figures S3 and S4), as is the maximum contribution to $J(\omega)$ between ^{1}H Larmor frequencies of 500 to 900 MHz (ca 5−6.5%; Supporting Information Tables S4 and S5). Outer-sphere relaxation also accounts for ^{1}H relaxivity NMRD data obtained with other nitroxides such as 2,2,6,6,-tetramethyl-1-piperidinyloxy (TEMPO) and 4-oxo-2,2,6,6-tetramethyl-1-piperidinyloxy (TEMPONE).[56−60] We therefore conclude that outer-sphere relaxation represents the dominant relaxation mechanism for nitroxide-based paramagnetic cosolutes and neglect any potential contributions from inner sphere relaxation (if such a relaxation mechanism for nitroxide-based cosolutes even exists for proteins, which seems highly unlikely from a structural perspective; see the second section of the Supporting Information for further discussion).

Limitations and Current Status of sPRE Analysis. Most theoretical descriptions of outer-sphere relaxation involve treating the nitroxide cosolute and protein as two hard-spheres (Figure 1), which are assumed to follow the Smoluchowski diffusion equation (see eq S4.1). Using the simple center-spin sphere model, Frezzatto et al.[61] showed that virtually identical spectral densities can be generated from different intermolecular potentials. For example, Figure 2A,B shows that the model parameters can be adjusted such that the spectral

https://doi.org/10.1021/jacs.2c10035
J. Am. Chem. Soc. 2022, 144, 21371−21388

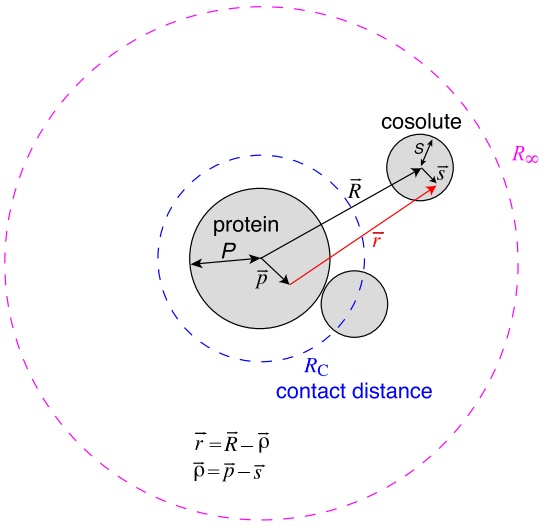

Figure 1. Diagrammatic representation of the hard sphere model of protein−cosolute interactions. The vector from the center of the protein to the center of the cosolute is denoted as $\vec{R}$; the vector from the center of the protein to the nucleus of interest is denoted as $\vec{p}$; and the vector from the center of the cosolute to the electron spin of interest is denoted as $\vec{s}$. The interspin distance is given by $\vec{r} = \vec{R} - \vec{\rho}$, where $\vec{\rho} = \vec{p} - \vec{s}$. The radius of the protein and cosolute are denoted as P and S. The contact distance is given by $R_C = P + S$. The outer boundary of the system is denoted as R_∞.

densities from the square-well potential and the force-free hard-sphere model are almost superimposable. This result demonstrates that the shape of the spectral densities may not be dependent on all the details of the potentials and dynamics of the cosolute and protein. One therefore cannot expect to construct a detailed picture of the intermolecular potential or of dynamics from the sPRE data alone.

We previously showed that it is possible to obtain the quantity $\langle r^{-6}\rangle_{\text{norm}}$, which represents a concentration-normalized equilibrium average of the interspin distance, defined by[20]

$$\langle r^{-6}\rangle_{\text{norm}} = 4\pi \int_0^\infty \frac{g(r)}{r^4}\mathrm{d}r \tag{9}$$

where r is the distance between the protein and cosolvent spins; $g(r)$ is the radial distribution function given by $\exp(-U(r)/k_BT)$, where $U(r)$ is the potential of mean force. $\langle r^{-6}\rangle_{\text{norm}}$ is determined not only by excluded volume interactions between the protein and cosolute but also by additional site-specific intermolecular forces arising from electrostatic and/or hydrophobic interactions. It should be noted that the factor of r^4 rather than r^6 is present in the denominator of the integral of eq 9 because the integrand is multiplied by r^2 arising from the volume element in spherical coordinates (i.e., $r^2\mathrm{d}\cos\theta\mathrm{d}\phi$). The component $\langle r^{-6}\rangle_{\text{norm}}^{\text{exc}}$, arising exclusively from the excluded volume of the protein and cosolute, can be directly calculated from the protein molecular coordinates. When $\langle r^{-6}\rangle_{\text{norm}}$ is larger than $\langle r^{-6}\rangle_{\text{norm}}^{\text{exc}}$, local attractive interactions are present, whereas when $\langle r^{-6}\rangle_{\text{norm}}$ is smaller than $\langle r^{-6}\rangle_{\text{norm}}^{\text{exc}}$, there are local repulsive interactions. Consequently, $\langle r^{-6}\rangle_{\text{norm}}$ can be used to identify the types of interactions (attractive, no force, or repulsive) between the cosolute and individual protons in a protein.

In principle, $\langle r^{-6}\rangle_{\text{norm}}$ could be determined if $J(\omega)$ were known at all frequencies using the inverse cosine transform of eq 2 at $t = 0$,

$$\langle r^{-6}\rangle_{\text{norm}} = \frac{C(0)}{n_S} = \frac{2}{n_S\pi}\int_0^\infty J(\omega)\mathrm{d}\omega \tag{10}$$

In practice, however, $J(\omega)$ can only be determined at a small number of frequencies owing to the limited availability of NMR spectrometer fields. In this regard, it is worth noting that Fries et al.[62] have proposed an interesting approach to extract multiple points on the spectral density using a single spectrometer field by changing the viscosity or temperature of the system. Although the latter approach seems to work reasonably well for small molecules, its extension to protein systems may not be straightforward as both protein conformation and stability are likely to be impacted by changes in the temperature or viscosity.

Our approach to the analysis of Γ_1 and Γ_2 sPRE data is based on fitting a few points on the spectral density curve using the ansatz:[20]

$$J_{\text{approx}}(\omega) = \frac{J(0)}{(1 + a\omega + b\sqrt{\omega})^2} \tag{11}$$

where b is given by

$$b = \frac{\sqrt{2}\,\pi n_S}{9D_{\text{trans}}^{3/2}J(0)} \tag{12}$$

Both a and b are adjustable fitted parameters: a is a site-specific parameter that varies from atom to atom in the protein; b is also site-specific but is obtained directly from the translational diffusion coefficient D_{trans} and the experimental, residue-specific values of $J(0)$ using eq 12. Therefore, we fit the experimental $J(\omega)$ data by optimizing residue-specific values of a and a global value of D_{trans}. Once a and b are determined with the spectral density given by eq 11, $\langle r^{-6}\rangle_{\text{norm}}$ can be obtained by evaluating the integral in eq 10. The mathematical form of the ansatz given in eq 11 has the desirable property that an analytic solution of the integral can be obtained and is given by

$$\langle r^{-6}\rangle_{\text{norm}} = \frac{16J(0)}{n_S\pi}\left[\frac{2(x_- - x_+) + (x_- + x_+)\ln(x_+/x_-)}{(x_+ - x_-)^3}\right] \tag{13}$$

where $x_\pm = -b \pm \sqrt{b^2 - 4a}$. Equation 13 provides an efficient method to obtain $\langle r^{-6}\rangle_{\text{norm}}$ once a and b are known.

The ansatz shown in eq 11 was tested for a system in which the cosolute and protein are represented as hard spheres in the presence of either a square-well or Coulombic potential (see Materials and Methods Section for more details) (Figure 2C,D). Figure 2D shows that $\langle r^{-6}\rangle_{\text{norm}}$ can be approximated reasonably well using the abovementioned procedures within errors of ∼20%. Figure 2C also shows that eq 11 fits the spectral density well even for the case that had the largest deviation (∼20%) from the exact $\langle r^{-6}\rangle_{\text{norm}}$ value (Figure 2D). The right panel of Figure 2C shows that the deviation arises from subtle differences at high frequencies, which suggest the practical limitions of our approach.

Once the residue(atom)-specific $\langle r^{-6}\rangle_{\text{norm}}$ values are known, one can calculate the effective residue-specific correlation times τ_C defined as

https://doi.org/10.1021/jacs.2c10035
J. Am. Chem. Soc. 2022, 144, 21371−21388

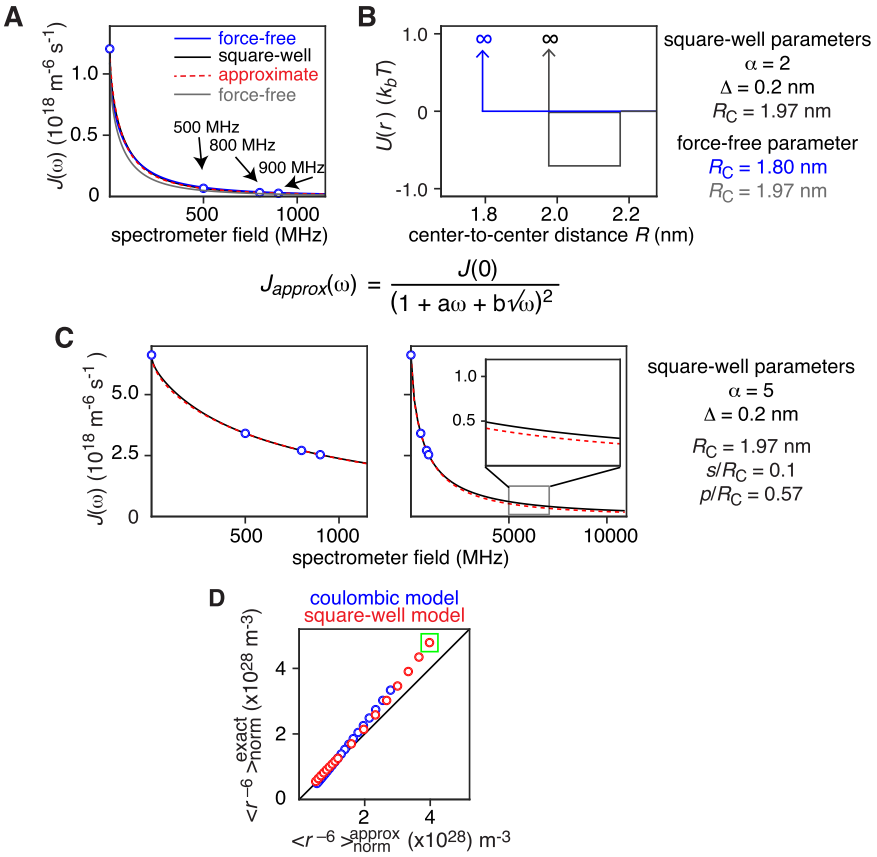

Figure 2. Properties of the spectral density function. (A) Spectral densities generated from the Force-Free Hard-Sphere (FFHS) model (blue, R_C = 18.7 Å and grey, R_C = 19.7 Å) and the hard-sphere model with a square-well potential (black, R_C = 19.7 Å). The approximate spectral density given by eq 11 is also plotted as a dashed red line. (B) Diagram depicting the intermolecular potentials used to generate spectral densities in panel A. The parameters for the FFHS model and the hard sphere model with a square well potential are also shown on the right. The spins are located at the centers of their respective spheres. (C) Exact (for hard-sphere square-well potential, black) and approximate (red dashed lines) spectral densities that showed the largest deviation of $\langle r^{-6}\rangle_{norm}$ among the models used in this study. The left panel shows that the approximate spectral density is virtually identical to the exact spectral density around the fitting points (500, 800, and 900 MHz). The right panel shows that the deviation comes from a subtle difference at high frequencies. (D) Correlation plot between exact and approximate $\langle r^{-6}\rangle_{norm}$ values. Results for the square-well potential (red) and Coulombic model (blue) with different parameters are plotted. For all simulations, the radii of the protein and nitroxide cosolute were set to 16.2 and 3.5 Å, respectively; T = 298 K, η = 0.89 cp, and n_S = 1 m^{-3}.

$$\tau_C = \frac{\int_0^\infty C(t)dt}{C(0)} = \frac{J(0)}{n_S\langle r^{-6}\rangle_{norm}} \quad (14)$$

τ_C is a measure of the timescale of the fluctuations of the interspin vector $\vec{r}$, which arise from both translational and rotational diffusion and are influenced by both short- and long-range intermolecular interactions.

We note that Fries[50] suggested a completely different approach for obtaining $\langle r^{-6}\rangle_{norm}$ for lanthanide paramagnetic metal ion complexes with very short T_{1e}, such as Yb^{3+} and Tb^{3+}. Fries' approach is based on the fact that for a paramagnetic cosolute with very short T_{1e}, eq 3 can be approximated by

$$J(\omega,T_{ie}) \approx C(0)\int_0^\infty \exp(t/T_{ie})dt = n_s\langle r^{-6}\rangle_{norm}T_{ie} \quad (15)$$

which is determined solely from the properties of the electron spin relaxation and is therefore independent of the molecular motion of the paramagnetic cosolute. Once T_{1e} is measured experimentally, $\langle r^{-6}\rangle_{norm}$ can then be easily extracted. However, as mentioned above, Curie relaxation is the dominant contribution to the overall relaxation for cosolutes with very short T_{ie}. Therefore, one may need to measure Γ_1 at very low external magnetic field (<1 T), where Curie relaxation is negligible, which requires the use of field cycling for both sensitivity and resolution purposes. Fries also proposed alternative ways of extracting $\langle r^{-6}\rangle_{norm}$ using relaxation data from several combinations of lanthanide paramagnetic complexes, and we refer the reader to the original paper[50] for details.

RESULTS AND DISCUSSION

In the Results and Discussion section, we present new insights into the interpretation of sPRE rates and the determination of various measures of residue-specific effective near-surface electrostatic potentials (ϕ_{ENS}) from sPRE data that exhibit different dependencies on distance and demonstrate the utility of these approaches to three model protein systems, two folded (ubiquitin and the folded state of the drkN SH3 domain) and one intrinsically disordered (the unfolded state of the drkN SH3 domain). (Note that the folded and unfolded states of drkN SH3 are approximately equally populated in solution, and exchange between these two states is slow on the chemical shift time scale, enabling one to study both states simultaneously under identical experimental conditions).[21,63]

https://doi.org/10.1021/jacs.2c10035
J. Am. Chem. Soc. 2022, 144, 21371−21388

The experimental results are then compared to theoretical results based on molecular coordinates using the Poisson-Boltzmann theory.

Properties of Γ_1 and Γ_2. The quantity $\langle r^{-6}\rangle_{norm}$ provides a rigorous and straightforward interpretation of the sPRE.[20] The calculation of $\langle r^{-6}\rangle_{norm}$ from our approach, however, based on the ansatz given by eq 11, requires accurate measurements of Γ_1 and Γ_2 for at least one field, and for Γ_1 at preferably multiple fields.[20] This is a potential drawback in instances where either Γ_1 or Γ_2 may be difficult to measure accurately. For example, when a proton spin is buried inside the protein interior, it is often the case that Γ_2 can still have quite large values, whereas the corresponding Γ_1 value may be too small to permit accurate measurement. While one could increase the concentration of nitroxide cosolute to increase the values of Γ_1, such an approach may result in significant line-broadening, owing to the corresponding increase in Γ_2 and would therefore suffer both in terms of spectral resolution and signal-to-noise. Because of these difficulties in measuring Γ_1 and/or Γ_2, $\langle r^{-6}\rangle_{norm}$ can potentially have large errors, or it may be impossible to obtain for some residues. Under such circumstances, it may therefore be preferable to analyze Γ_1 or Γ_2 separately and still obtain some meaningful physical information. We explore this possibility in this section.

We first investigate how Γ_1 and Γ_2 change as a function of spin location using the FFHS model.[54,55] Figure 3A,B display the relative Γ_1, Γ_2, and $\langle r^{-6}\rangle_{norm}$ values as a function of different spin locations within a protein described by p, the distance between the spin location and the center of the protein sphere. Γ_2 and $\langle r^{-6}\rangle_{norm}$ both increase as the spin location becomes exposed to the solvent, but the increase in Γ_2 is much less pronounced when compared to that of $\langle r^{-6}\rangle_{norm}$ (Figure 3A). Γ_1, however, increases either less or more rapidly than $\langle r^{-6}\rangle_{norm}$, depending on spectrometer field (Figure 3B).

An intuitive explanation for the different behaviors of Γ_1, Γ_2, and $\langle r^{-6}\rangle_{norm}$ is as follows. First, the probability of finding a cosolute molecule at a distance r from the protein scales with r^2. Thus, the probability of finding cosolute molecules at long r is higher than at short r, and hence, the dipolar interaction between a proton spin on the protein and an electron spin on the cosolute is more long-range in nature. Second, $J(0)$ accounts for most of the contribution to Γ_2. From eq 2, it is easy to see that $J(0)$ represents the area under the correlation function $C(t)$ from $t = 0$ to infinity. It follows that the trajectories of diffusing cosolutes at long time periods contribute significantly to $J(0)$. At a long time period, cosolute molecules that are initially close to the protein surface can diffuse away at some point and come back to the surface of the protein at a later time. Such re-encounter processes can be repeated many times over and result in a significant contribution to $J(0)$.[39,64] That is, diffusive motion when cosolute and protein are apart plays a critical role in determining the reencounter probability and hence is important in determining the value of $J(0)$. As a result, the scaling of $J(0)$ with distance is less than that of $\langle r^{-6}\rangle$. $J(\omega)$ or Γ_1 at high frequency, however, pertain to the rapid oscillatory behavior of the dipolar interactions between nuclear and electron spins. Thus, only events that involve a sudden change in the dipolar fields experienced by the protein spin contribute to $J(\omega)$ at high frequency. As one can see from Figure S1B, the dipolar field gradients become steeper as the interspin distance gets shorter, and a slight change in the interspin distance at short distances can result in a large change in the magnetic field experienced by the protein spins (see Figure S1C). Consequently, $J(\omega)$ mostly reports on the interaction of the cosolute near the protein spin, resulting in a distance dependence that scales by more than $\langle r^{-6}\rangle$ at high spectrometer field. A more detailed discussion of the distance dependence of the spectral densities is presented below, as well as in Sections S4 and S5 of the Supporting Information.

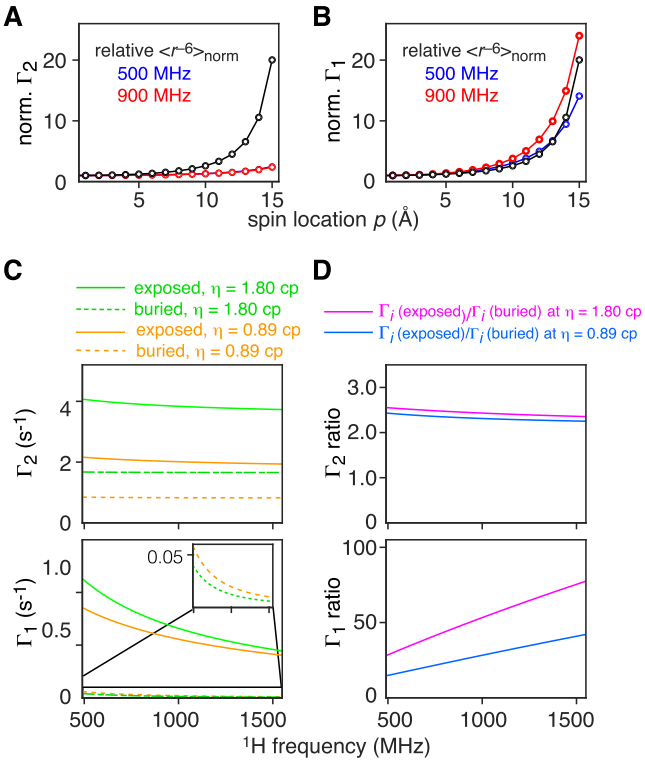

Figure 3. Properties of Γ_1 and Γ_2 for the Force-Free Hard-Sphere (FFHS) model. Dependence of normalized (A) Γ_1 and (B) Γ_2 on the spin location at two spectrometer fields (500 and 900 MHz); also shown is the relative $\langle r^{-6}\rangle_{norm}$ in black. Γ_1, Γ_2, and $\langle r^{-6}\rangle_{norm}$ are normalized relative to the corresponding values when the proton spin is located at the center of the sphere (i.e., $p = 0$ Å). The parameters used in these simulations are as follows: $R_C = 19.7$ Å, $s = 2$ Å, $p = 15.2$ Å, $T = 298$ K, $n_S = 25$ mM, and $\eta = 0.89$ cp. (C) Γ_1 and Γ_2 at $\eta = 0.89$ cp (green) and 1.80 cp (orange) as a function of spectrometer field. The protein spin is located at either $p = 15.2$ or 0 Å for exposed (solid line) or buried (dashed line) locations, respectively. The inset in the Γ_1 plot shows an expanded view for a buried spin delineated by the boxed region. (D) Relative values of Γ_1 and Γ_2 at $\eta = 0.89$ cp (cyan) and 1.80 cp (magenta) as a function of spectrometer field. That is, the values of Γ_1 and Γ_2 of the exposed spin at given viscosities are divided by the corresponding value for the buried spin. The other parameters used in panels (C) and D) are as follows: $R_C = 19.7$ Å, $s = 2$ Å, and $T = 298$ K, and the concentration of nitroxide cosolute is set to 25 mM.

To ascertain how the dynamics of cosolute diffusion affect the sPRE, we consider the effect of viscosity on Γ_1 and Γ_2. The proton spin is placed at two different locations: at the center (buried) of the sphere and on the surface (exposed). Figure 3C shows that Γ_2 is only weakly dependent on the spectrometer field and scales approximately with viscosity for both buried (dashed line) and exposed spins (solid line). Γ_1, on the other hand, varies significantly with both the spectrometer field and viscosity. The Γ_2 ratios between buried and exposed spins are approximately the same for different viscosities (Figure 3D). However, the corresponding Γ_1 ratio differs significantly between the two viscosities and varies with the spectrometer

https://doi.org/10.1021/jacs.2c10035
J. Am. Chem. Soc. 2022, 144, 21371−21388

field (Figure 3D). The very weak dependence on spectrometer field (at 500 MHz or higher) and viscosity for the Γ_2 ratio is due to the fact that the field independent term $J(0)$ is the predominant contributor to Γ_2 (eq 8), while Γ_1 is dependent on $J(\omega)$ (eq 7).

Moreover, the relative values of $J(0)$ are insensitive to changes in the values of T/η. This result is expected in our theoretical framework where protein and cosolutes are assumed to diffuse and collide according to the Smoluchwoski Equation given by eq S4.1 because $J(0)$ is linearly proportional to the translational diffusion constant D_{trans} (see eq S6.30), regardless of spin location or strength of the potential. If the potential of mean force is independent of T/η then $J(0)$ is linearly proportional to η/T. Hence, the relative values of Γ_2, which are proportional to $J(0)$, are insensitive to both changes in the spectrometer field and translational diffusion constant. Thus, Γ_2 provides a more experimentally practical quantity for analysis than Γ_1, which depends significantly on both the diffusion constant and spectrometer field in a complex way. It should also be pointed out that, in the context of the sPRE, Γ_2 is easier to measure in practice, as Γ_2 is much larger than Γ_1 (due to $J(0) \gg J(\omega)$).

Next, we investigate the physical meaning of $J(0)$. It has been pointed out by Halle[41] that spin relaxation arising from dipole−dipole interactions in the low-frequency regime is long-range in nature. That is, cosolute molecules located far from the protein still contribute significantly to $J(0)$. To illustrate this point, we calculate the contribution of cosolute−protein interactions initially distributed at a distance R_o above some distance R_a (i.e., $R_a < R_o$) on $J(0)$. For proton and electron spins located at the center of the protein and nitroxide cosolute, respectively, the relative contribution of cosolute molecules at long distance is given by (see Section S4 in the Supporting Information for derivations)

$$\frac{J(0, R_a < R_o)}{J(0)} = \frac{1}{8}\left(\frac{R_C}{R_a}\right)\left(9 - \left(\frac{R_C}{R_a}\right)^2\right) \tag{16}$$

where R_C is the contact distance between the protein and cosolute. Thus, at long distances, the $J(0)$ contribution scales proportional to R_C/R_a, indicative of the long-range nature of the interactions.

The ratio $J(0, R_a < R_o)/J(0)$ and $J(\omega, R_a < R_o)/J(\omega)$ for ν = 500 and 900 MHz are plotted in Figure 4A. It can be seen that the contribution of short-range interactions becomes increasingly dominant for $J(\omega)$ at high spectrometer frequencies. Thus, $J(\omega)$ can be short-range in nature, especially at high fields. In other words, Γ_1 measured at high spectrometer fields contains more information about the local environment around the nucleus than $J(0)$ or $\langle r^{-6}\rangle_{norm}$; however, the physical interpretation of Γ_1 is not straightforward as discussed above. A more elaborate discussion of the distance and frequency dependence of $J(\omega)$ can be found in refs 41 and 65.

It is worth noting that if rotational motion of the protein and cosolute are described by the Stoke−Einstein relation (see eqs S3.12 and S3.13), $J(0)/D_{trans}$ is determined only by structural properties, such as the molecular radii of the cosolute and protein and the location of the nuclear and electron spins. For nuclear and electron spins located at the center of the protein and nitroxide cosolute, respectively, $J(0)$ for the FFHS model is given exactly by $16\pi n_S/27D_{trans}R_C$, which can be rewritten as

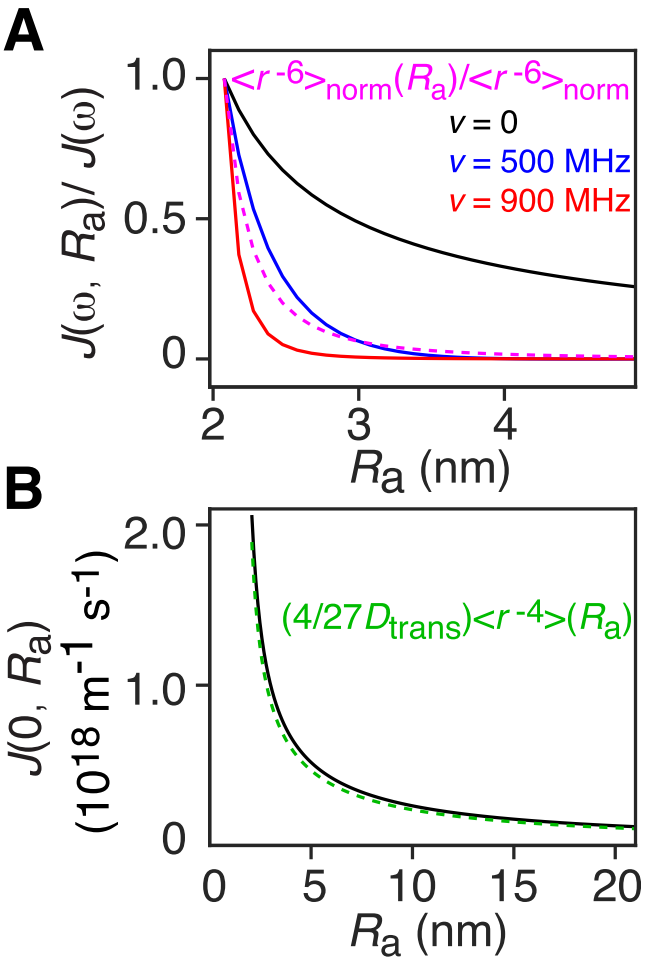

Figure 4. Dependence of the spectral densities on distance. (A) Normalized spectral densities defined by the ratio of the partial spectral densities $J(0, R_a < R_o)/J(0)$ and $J(\omega, R_a < R_o)/J(\omega)$ for the FFHS model as a function of some cut-off distance R_a. The calculation was performed using eqs S4.24 and S5.11. This plot shows the contributions of the spectral densities for the cosolute initially located at $R_a < R_o$ for ν = 0 (black), 500 (blue), and 900 (red) MHz. For comparison, the normalized $\langle r^{-6}\rangle_{norm}(R_a)/\langle r^{-6}\rangle_{norm}$, where $\langle r^{-6}\rangle_{norm}(R_a)$ defined by eq S7.7, is also plotted to give a sense of the distance dependence of $\langle r^{-6}\rangle_{norm}$. (B) Comparison between absolute values of $J(0, R_a < R_o)$ (black line) and $(4N_S/27D_{trans})\langle r^{-4}\rangle_{norm}(R_a)$ (green dashed line) for the FFHS model. For all simulations in this figure, the contact distance is set to R_C = 19.7 Å; T = 298 K, η = 0.89 cp, and n_S = 1 m^{-3}; the location of the nuclear and electron spins on the protein and nitroxide cosolute, respectively, is set to p = 15.2 Å and s = 2 Å.

$$J(0) = \frac{4n_S}{27D_{trans}}\langle r^{-4}\rangle_{norm} \tag{17}$$

since $\langle r^{-4}\rangle_{norm} = 4\pi\int_{R_C}^{\infty}\frac{g(r)}{r^2}dr = \frac{4\pi}{R_C}$ when $g(r) = 1$ for $R_C > 0$ and 0 for $R_C < 0$ (i.e., the hard sphere model).

Equation 17 also provides a reasonable approximation for $J(0)$ even when the nuclear and electron spins are located off-center (see Figure 5A). For a square-well potential of depth α and length R_b (see Material and Methods Section, eq 31), $J(0)$ can be approximated by eq 17 when $\Delta\alpha = \alpha - 1$ is small (see Section S.4 in the Supporting Information for details) (Figure 5B and Supporting Information Figure S5). In addition, we

https://doi.org/10.1021/jacs.2c10035
J. Am. Chem. Soc. 2022, 144, 21371−21388

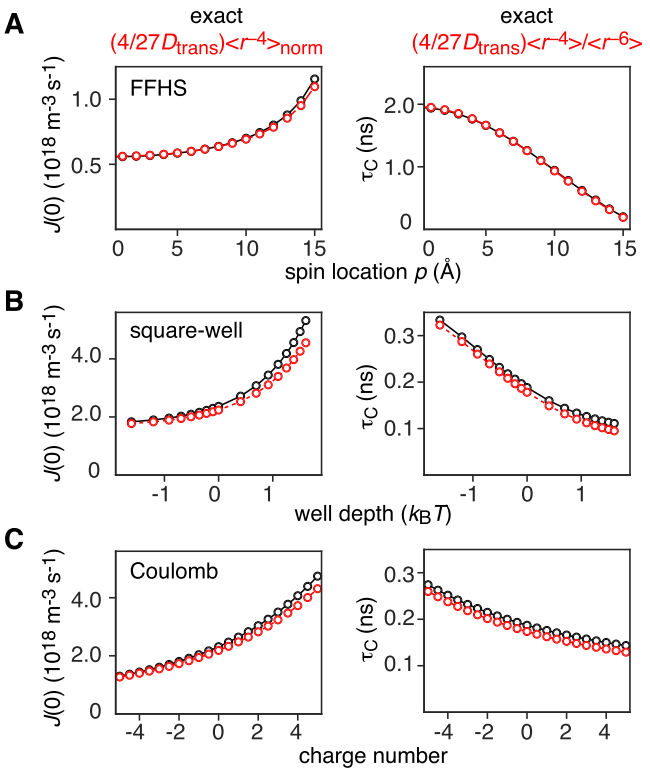

Figure 5. Comparison between exact and approximate $J(0)$ and τ_C from eq 17. (A) $J(0)$ and τ_C from the FFHS model are plotted as a function of the proton spin location given by the distance from the proton to the center of the protein (denoted as p). The larger the value of p, the closer is the proton to the surface of the protein. $J(0)$ and τ_C are also plotted as a function of (B) well-depth for the square-well potential model (eq 31 in the Material Methods Section) and (C) protein charge for a Coulomb potential model (eq 32 in the Material and Methods Section). For all simulations in this figure, the contact distance is set to R_C = 19.7 Å; T = 298 K, η = 0.89 cp, and n_S = 1 m^{-3}; and the location of the nuclear spin in the protein and the electron spin in the nitroxide cosolute are set to p = 15.2 Å and s = 2 Å, respectively. In (C), the Coulomb potential is proportional to the product of the protein charge (placed at the center of the sphere) and the charge on the cosolute (set to −1).

investigated the effect of Colombic interactions (see Material and Methods Section, eq 32) by simulating the dependence of $J(0)$ on protein charge with a fixed cosolute charge of −1 (Figure 5C). Again, eq 17 provides an excellent approximation of $J(0)$ over a range of protein charges (Figures 5C and Supporting Information S5). Finally, when $(4/27D_{trans})\langle r^{-4}\rangle_{norm}(R_a)$, defined by eq S7.7, is plotted against $J(0, R_a < R_o)$ for the FFHS model, excellent agreement is also observed (Figure 5A), indicating that $J(0)$ is indeed related to $\langle r^{-4}\rangle_{norm}$.

In summary, we find that $J(0)$ is inversely proportional to D_{trans} and may also be related to $\langle r^{-4}\rangle_{norm}$ through the approximation given in eq 17. We note, however, that we only carried out simulations for simple sphere models with a spherically symmetric potential and a single diffusion constant rather than a more physically realistic model with arbitrary shapes of the molecule and arbitrary potentials and possibly with a distance-dependent diffusion constant.

Impact of Intermolecular Potentials on the Apparent Overall Correlation Time (τ_C). Our analysis also yields an apparent correlation time τ_C defined by eq 14. It should be emphasized that τ_C depends not only on translational diffusion but also on the intermolecular interactions in a complicated fashion. At a first glance, it seems tempting to relate τ_C with "residence time" of the cosolute on the protein, that is the mean time taken for a cosolute to reach an outer boundary of the interaction region.

In the framework of inner- and second-sphere relaxation mechanisms for a paramagnetic metal ion, τ_C is given by[12,30,66−69]

$$\tau_C^{-1} = \tau_R^{-1} + \tau_M^{-1} + T_{i,e}^{-1} \tag{18}$$

where τ_R is the rotational correlation time of the protein; τ_M the residence time of the cosolute; and $T_{i,e}^{-1}$ with i = 1,2 are the longitudinal and transverse electron relaxation rates, respectively. The approximation provided by eq 18 is applicable for a paramagnetic cosolute that forms a weak, rotationally correlated complex with the protein.[69−71] For the second-sphere relaxation model, it is often assumed that τ_M is determined by the properties of the cosolute (e.g., translational diffusion constant), and hence, τ_C is assumed to be same over the entire protein surface.[12,72] For outer-sphere relaxation, this assumption does not hold, and τ_C varies with spin location (see Figure 5), as is found to be the case experimentally with nitroxide cosolute−protein interactions.[20,21]

In the case of the FFHS model with the nuclear and electron spins located at the center of the protein and cosolute, respectively, τ_C is can be expressed as

$$\tau_C = \frac{4}{27D_{trans}} \frac{\langle r^{-4}\rangle_{norm}}{\langle r^{-6}\rangle_{norm}} \tag{19}$$

Equation 19 is a straightforward consequence of substituting eq 17 into eq 14. As shown in the right-hand panels of Figure 5, eq 19 is a good approximation for the different interaction potentials studied here.

From eq 19, τ_C is inversely proportional to the translational difusion constant D_{trans}. Importantly, τ_C also depends on the interaction potential through the ratio $\langle r^{-4}\rangle_{norm}/\langle r^{-6}\rangle_{norm}$. For an interaction potential that decays to 0 at large interspin distance, the latter ratio becomes smaller for attractive and larger for repulsive interactions. As a result, τ_C values for different cosolutes can be significantly different even when the translational difusion constants of the cosolutes are the same. Indeed, from our calculations using eq 19, we obtain *shorter* τ_C values as the interaction between cosolute and protein becomes more attractive. This result may appear counter-intuitive if one's interpretion of τ_C is based on inner- or second-sphere relaxation described by eq 18 since an attractive interaction, in this instance, will result in a longer residency time τ_M for the cosolute in the vicinity of the protein.

Studying Electrostatic Interactions by sPRE. The sPRE has been used to study electrostatics on the surface of proteins,[28,73] monosaccharides,[74] membranes[22,24,25] and other small molecules.[26] For example, Likhtenshtein et al.[26] measured the ratio of Γ_1 values obtained with charged (positive or negative) and neutral nitroxide-based cosolutes for various small molecules and interpreted the resulting data using Freed's approximation[54,75] (see eq 4.2 in ref 54) for comparison with the average electrostatic potential, calculated using the classical Debye equation, in the vicinity of the proton of interest.

Recently, Yu et al.[28,29] developed a new interpretation of the sPRE measured for oppositely charged nitroxide-based

https://doi.org/10.1021/jacs.2c10035
J. Am. Chem. Soc. 2022, 144, 21371−21388

cosolutes. We briefly review their approach, and then extend it to other experimental sPRE-derived measures of electrostatics that provide information ranging from short- to long-range interactions.

The central quantity of interest is the experimental effective near-surface electrostatic potential (ϕ_{ENS}) which Yu et al.[28] defined as

$$\phi_{ENS}^{\Gamma_2} = -\frac{k_B T}{2e} \ln \frac{\Gamma_2^{+ve}}{\Gamma_2^{-ve}} \quad (21)$$

where e is the electron charge, Γ_2^{+ve} and Γ_2^{-ve} are the Γ_2 values obtained using positively and negatively charged nitroxide-based cosolutes, respectively. It is important to note that all Γ_2 rates have to be obtained at or normalized to the same cosolute concentration. The interpretation of the $\phi_{ENS}^{\Gamma_2}$ potential by Yu et al.[28,29] is based on eqs 9 and 14, and is given by

$$\phi_{ENS}^{\Gamma_2} = -\frac{k_B T}{2e} \ln \frac{\langle r^{-6}\rangle_{norm}^{+ve}}{\langle r^{-6}\rangle_{norm}^{-ve}} \frac{\tau_C^{+ve}}{\tau_C^{-ve}} \quad (22)$$

where $\langle r^{-6}\rangle_{norm}^{\pm ve}$ and $\tau_C^{\pm ve}$ are the $\langle r^{-6}\rangle_{norm}$ and τ_C values measured in the presence of positively or negatively charged cosolutes, respectively. Yu et al.[28,29] then assumed that the ratio of τ_C^{+ve} to τ_C^{-ve} is ~1 for all residues and obtained the approximate relationship

$$\phi_{ENS}^{\Gamma_2} \approx -\frac{k_B T}{2e} \ln \frac{\langle r^{-6}\rangle_{norm}^{+ve}}{\langle r^{-6}\rangle_{norm}^{-ve}} \quad (23)$$

where the left hand-side of the equation is the approximate experimental ϕ_{ENS} potential derived from the ratio of Γ_2 values (see eq 21), and the right-hand side of the equation represents the exact definition of the experimental ϕ_{ENS} potential based on eq 9.

The central tenet of the analysis by Yu et al.[28,29] is the approximation that all interactions other than electrostatic interactions cancel out when the charged nitroxide cosolutes are similar in structure and that $\tau_C^{+ve} = \tau_C^{-ve}$. In their study, the nitroxide-based cosolutes employed were 2,2,5,5-tetramethyl-1-pyrrolidinyloxy (PROXYL) derivatives, specifically 3-carboxy PROXYL and 3-aminomethyl PROXYL for negatively and positively charged cosolutes, respectively.

The experimental $\phi_{ENS}^{\Gamma_2}$ obtained using eq 21 was then interpreted by comparison with the idealized Poisson-Boltzman potential, ϕ_{ENS}^{PB}, where only excluded volume and electrostatic interactions are taken into account, given by[28]

$$\phi_{ENS}^{PB} = -\frac{k_B T}{2e} \ln \frac{\int r^{-6} \exp\left(-\frac{\phi_{elec}^{+ve}(\vec{q})}{k_B T}\right) d\vec{q}}{\int r^{-6} \exp\left(-\frac{\phi_{elec}^{-ve}(\vec{q})}{k_B T}\right) d\vec{q}} \quad (24)$$

where $\vec{q}$ are the coordinates that specify the interspin vector $\vec{r}$ (i.e., interspin distance and relative orientation of the protein and cosolute); $\phi_{elec}^{\pm ve}(\vec{q})$ is the electrostatic potential at $\vec{q}$. The integral in eq 24 is taken over the protein excluded space that can be occupied by the nitroxide cosolute. The superscript "PB" denotes the fact that Poisson-Boltzmann theory[76,77] is used to simulate the electrostatic interactions. Equation 24 can be computed from the molecular coordinates of the protein under investigation (see Material and Methods Section). Yu et al.[28] found good agreement between the experimental $\phi_{ENS}^{\Gamma_2}$ determined from the ratio of Γ_2 values for positive and negative cosolutes measured for both ubiquitin and the Antp homeodomain-DNA complex and the corresponding theoretical ϕ_{ENS}^{PB} values.

The experimental and theoretical definitions of ϕ_{ENS} provided by eqs 21 and 24 involve the use of a positively charged paramagnetic cosolute, such as 3-aminomethyl PROXYL.[28] The pure form of the latter, however, is a highly viscous gel-like substance, whose concentration is hard to quantify in terms of weight (although NMR can also be used to determine its concentration[28,78]). In the context of PROXYL-based cosolutes, from a purely practical perspective, we found it more convenient experimentally to employ the neutral paramagnetic cosolute, 3-carbamoyl-PROXYL (Figure 6A), that we used in our previous sPRE studies.[20,21] Analogous expressions for the experimental and theoretical ϕ_{ENS}

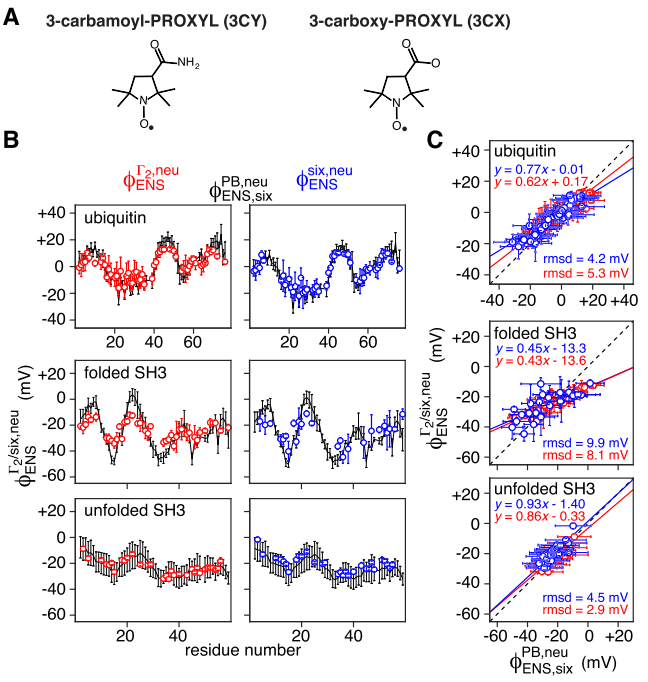

Figure 6. Experimental assessment of the effective near-surface electrostatic potential (ϕ_{ENS}) for three model protein systems: ubiquitin and the native (folded) and unfolded states of drkN SH3. (A) Structures of 3-carbamoyl PROXYL (3CY) and 3-carboxy PROXYL (3CX) nitroxide-based cosolutes. (B) Comparison of the experimental $\phi_{ENS}^{\Gamma_2,neu}$ (red circles) and $\phi_{ENS}^{six,neu}$ (blue circles) potentials with the theoretical Poisson-Boltzmann $\phi_{ENS,six}^{PB,neu}$ (black lines) potentials for three proteins: ubiquitin and native (folded) drkN SH3 and unfolded drkN SH3. The Γ_2 data were measured at a spectrometer frequency of 500 MHz. (C) Corresponding correlation plots of $\phi_{ENS,six}^{PB,neu}$ versus $\phi_{ENS}^{\Gamma_2,neu}$ (magenta) and $\phi_{ENS}^{six,neu}$ (green). Error bars represent 1 S.D.; rmsd, root mean square deviation. The error bars for $\phi_{ENS}^{\Gamma_2,neu}$ and $\phi_{ENS}^{six,neu}$ are obtained by standard error propagation of the measured experimental errors. The errors for $\phi_{ENS,six}^{PB,neu}$ are obtained by taking one standard deviation of the $\phi_{ENS,six}^{PB,neu}$ potential generated from an ensemble of 50 structures calculated for ubiquitin and the native state drkN SH3 and 100 structures for the unfolded state drkN SH3 (see Materials and Methods Section). Errors bars represent 1 S.D. The values of $\phi_{ENS,six}^{PB,neu}$ were shifted vertically to minimize the rmsd between experimental and theoretical ϕ_{ENS} profiles (see Table S6).

https://doi.org/10.1021/jacs.2c10035
J. Am. Chem. Soc. 2022, 144, 21371−21388

potentials provided by eqs 21 and 24 in the case of negatively charged and neutral nitroxide cosolutes are

$$\phi_{ENS}^{\Gamma_2,neu} = -\frac{k_B T}{e}\ln\frac{\Gamma_2^{neu}}{\Gamma_2^{-ve}} \quad (25)$$

$$\phi_{ENS,six}^{PB,neu} = -\frac{k_B T}{e}\ln\frac{\int r^{-6}d\vec{q}}{\int r^{-6}\exp\left(-\frac{\phi_{elec}^{-ve}(\vec{q})}{k_B T}\right)d\vec{q}} \quad (26)$$

where the superscript "neu" has been added to distinguish between the ϕ_{ENS} potential defined in eqs 21 and 24, and the subscript 'six' in eq 26 denotes that r^{-6} is used to calculate the theoretical ϕ_{ENS} potential. Further, since our analysis of sPRE data using eqs 11−13 provides a direct experimental determination of $\langle r^{-6}\rangle_{norm}$ (through the measurement of Γ_2 at one field and Γ_1 at multiple fields), we define an exact (given eq 9) experimentally accessible definition of the ϕ_{ENS} potential given by

$$\phi_{ENS}^{six,neu} = -\frac{k_B T}{e}\ln\frac{\langle r^{-6}\rangle_{norm}^{neu}}{\langle r^{-6}\rangle_{norm}^{-ve}} \quad (27)$$

where the superscript "six" denotes that the ratio of $\langle r^{-6}\rangle_{norm}$ for neutral and negatively charged nitroxide cosolutes used to calculated the ϕ_{ENS} potential.

Here, we investigate the validity of the two central assumptions of Yu et al.[28] that (1) $\tau_C^{+ve} \approx \tau_C^{-ve}$, and (2) the experimentally derived $\phi_{ENS}^{\Gamma_2,neu}$ or $\phi_{ENS}^{six,neu}$ potentials can be interpreted in terms of the theoretical $\phi_{ENS,six}^{PB,neu}$ potential calculated from molecular coordinates.

Regarding the first assumption, it can be seen in Figure 5C that, for a simple Coulomb hard sphere model, τ_C varies significantly as a function of protein charge (with the charge on the cosolute set to −1; for a cosolute with charge +1, the x axis in Figure 5C would be inverted). For the model parameters used in Figure 5C, the ratio $\tau_C^{+ve}/\tau_C^{-ve}$ for a protein with charge +5 (or −5) is approximately 2. Thus, the assumption that $\tau_C^{+ve} \sim \tau_C^{-ve}$ does not hold in general. The relevant ratios for $\phi_{ENS}^{\Gamma_2,neu}$ are either $\tau_C^{+ve}/\tau_C^{neu}$ or $\tau_C^{neu}/\tau_C^{-ve}$ (depending on whether the charged cosolute is positive or negative, respectively). For the parameters in Figure 5C, with a protein of charge +5, $\tau_C^{+ve}/\tau_C^{neu}$ and $\tau_C^{neu}/\tau_C^{-ve}$ have values of ∼0.68 and ∼0.76, respectively, much closer to 1 than the ratio obtained using positively and negatively charged cosolutes. Thus, the assumption that τ_C is the same for both cosolutes holds better for $\phi_{ENS}^{\Gamma_2,neu}$ than for $\phi_{ENS}^{\Gamma_2}$.

To ascertain the validity of the second assumption, we calculated $\phi_{ENS,six}^{PB,neu}$ in the presence of a simple square-well potential (see eq 31 in Material and Methods section for details) that roughly mimics short-range atomic interactions. We denote the analog of eq 26 in the presence of a square-well potential as $\phi_{ENS,six}^{PB+SQ,neu}$. If short-range interactions do not affect the value of $\phi_{ENS,six}^{PB,neu}$, $\phi_{ENS,six}^{PB,neu}$, and $\phi_{ENS,six}^{PB+SQ,neu}$ should be the same. As shown in Supporting Information Figure S6, $\phi_{ENS,six}^{PB,neu}$ and $\phi_{ENS,six}^{PB+SQ,neu}$ are in good qualitative agreement for three model protein systems: ubiquitin and native and unfolded states of drkN SH3 (as the calculated values of $\phi_{ENS,six}^{PB,neu}$ are essentially identical whether the nitroxide cosolutes are represented as hard spheres or by full atomic representations; see Supporting Information Figure S7). A few residues, however, are significantly impacted (>10 mV) by the presence of short-range interactions, although the majority exhibit only minor discrepancies (<5 mV). Hence some degree of caution should be used with respect to any quantitative interpretation of experimental ϕ_{ENS} potentials.

The considerations discussed above notwithstanding, the experimentally derived $\phi_{ENS}^{\Gamma_2,neu}$ values agree well with their theoretical $\phi_{ENS,six}^{PB,neu}$ counterparts for all three model protein systems (Figure 6). In our analysis, the root mean square difference (rmsd) between theoretical and experimental ϕ_{ENS} potentials was minimized by vertically shifting the theoretical ϕ_{ENS}^{PB} profile to take account of any systematic uncertainties, including inaccuracies in ionic strength or cosolute concentration (see Supporting Information Tables S6 and S7). Perhaps surprisingly, the theoretical $\phi_{ENS,six}^{PB,neu}$ values for the unfolded state of the drkN SH3 calculated using the structural ensemble obtained from a temperature replica exchange molecular dynamics simulation[21] are in excellent agreement with both the experimental $\phi_{ENS}^{six,neu}$ and $\phi_{ENS}^{\Gamma_2,neu}$ values. Further, the up and down features of the ϕ_{ENS} potential for unfolded drkN SH3 (from −30 to 0 mV) are less pronounced than those in the folded state (−45 to 0 mV). This is expected given that the unfolded state can adopt many different conformations with different charge distributions on the surface of the polypeptide chain. As a result, the variation in average charge distribution over the surface of the unfolded polypeptide ensemble is considerably reduced relative to the native state. Figure S8 shows that a number of residues for the two folded protein systems have $\tau_C^{neu}/\tau_C^{-ve}$ ratios that deviate from a value of 1, but in the case of the unfolded state of drkN SH3, almost all residues have a $\tau_C^{neu}/\tau_C^{-ve}$ ratio very close to 1, which accounts for the almost perfect match of $\phi_{ENS}^{\Gamma_2,neu}$ and $\phi_{ENS}^{six,neu}$ values for the unfolded state.

We also investigated the possibility of using experimentally determined $J(0)$ values to analyze electrostatic interactions based on the approximation given by eq 17. We introduce two new quantities given by

$$\phi_{ENS}^{J(0),neu} = -\frac{k_B T}{e}\ln\frac{2\Gamma_2^{neu} - \Gamma_1^{neu}}{2\Gamma_2^{-ve} - \Gamma_1^{-ve}} = -\frac{k_B T}{e}\ln\left(\frac{J^{neu}(0)}{J^{-ve}(0)}\right) \quad (28)$$

and

$$\phi_{ENS,four}^{PB,neu} = -\frac{k_B T}{e}\ln\frac{\int r^{-4}d\vec{q}}{\int r^{-4}\exp\left(-\frac{\phi_{elec}^{-ve}(\vec{q})}{k_B T}\right)d\vec{q}} \quad (29)$$

Figure 7 compares the experimental $\phi_{ENS}^{J(0),neu}$ values with the corresponding theoretical $\phi_{ENS,four}^{PB,neu}$ and $\phi_{ENS,six}^{PB,neu}$ values. For the two folded proteins, ubiquitin and the native state of drkN SH3, the theoretical $\phi_{ENS,four}^{PB,neu}$ potential agrees more closely with the experimental $\phi_{ENS}^{J(0),neu}$ potential. For the unfolded state of drkN SH3, however, slightly better agreement is observed between the experimental $\phi_{ENS}^{J(0),neu}$ and theoretical $\phi_{ENS,six}^{PB,neu}$ potentials. A possible explanation for these observations is as follows. In a folded protein, the backbone is essentially fixed and conformational mobility of surface side chains gives rise to only minor variations in the effective near-surface electrostatic potential. As a result, the experimental $\phi_{ENS}^{J(0),neu}$ is likely to be dominated by long-range electrostatic interactions. For an intrinsically disordered protein, such as the unfolded state of drkN SH3, however, the molecular surface is highly variable as an infinite number of backbone configurations, including

https://doi.org/10.1021/jacs.2c10035
J. Am. Chem. Soc. 2022, 144, 21371−21388

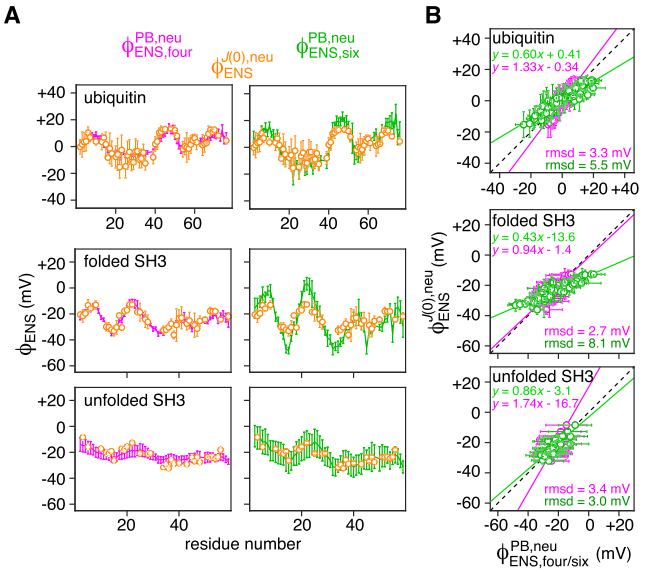

Figure 7. Alternative interpretation of the ϕ_{ENS} potential based on $\langle r^{-4}\rangle_{norm}$. (A) Comparison of experimental $\phi_{ENS}^{J(0),neu}$ values (orange circle) to the theoretical $\phi_{ENS,four}^{PB,neu}$ (magenta line; left panels) and $\phi_{ENS,six}^{PB,neu}$ (green line, right panels) values for ubiquitin (top) and native (folded) drkN SH3 (middle) and unfolded drkN SH3 (bottom panel). (B) Corresponding correlation plots of $\phi_{ENS}^{J(0),neu}$ versus $\phi_{ENS,four}^{PB,neu}$ (magenta) and $\phi_{ENS,six}^{PB,neu}$ (green). Error bars represent 1 S.D.; rmsd, root mean square deviation. $\phi_{ENS,four}^{PB,neu}$ and $\phi_{ENS,six}^{PB,neu}$ were shifted vertically to minimize the rmsd between experimental and theoretical ϕ_{ENS} profiles (see Table S7).

transient close contacts between residues far apart in the amino acid sequence, can be adopted, with consequent very large differences between the effective near-surface electrostatic potentials of the individual conformers within the unfolded ensemble. Under such conditions, the ensemble average contribution to $\phi_{ENS}^{J(0),neu}$ from longer range electrostatic interactions between the unfolded protein and the nitroxide cosolute may be diminished, as the contributions from individual members of the ensemble are partially cancelled out. The contribution from shorter range electrostatic interactions to $\phi_{ENS}^{J(0),neu}$, on the other hand, involves individual residues or sets of neighboring residues in the sequence and therefore would be predicted to exhibit much less variability between the different conformers of the unfolded ensemble. As a corollary, while the theoretical Poisson-Boltzmann $\phi_{ENS,four}^{PB,neu}$ and $\phi_{ENS,six}^{PB,neu}$ potentials are easily calculated from the molecular coordinates of a folded protein, it is likely that the accuracy of the theoretical $\phi_{ENS,four}^{PB,neu}$ potential for an unfolded protein may suffer from undersampling of the full range of conformations, as it is only feasible to carry out the Poisson-Boltzmann calculations with a limited number of snapshots from the replica exchange molecular dynamics trajectory.

Finally we calculated the $\phi_{ENS}^{\Gamma_1,neu}$ potential from Γ_1

$$\phi_{ENS}^{\Gamma_1,neu} = -\frac{k_B T}{e}\ln\frac{\Gamma_1^{neu}}{\Gamma_1^{-ve}} = -\frac{k_B T}{e}\ln\left(\frac{J^{neu}(\omega_H)}{J^{-ve}(\omega_H)}\right) \quad (30)$$

which is analogous to the approach taken by the Likhtenshtein et al.[26] Figure S9 shows that the experimental $\phi_{ENS}^{\Gamma_1,neu}$ profiles are very similar to those of the theoretical $\phi_{ENS,six}^{PB,neu}$ profiles for all three model protein systems. This is expected as $\phi_{ENS}^{six,neu}$ and $\phi_{ENS}^{\Gamma_1,neu}$ both contain more local information near the proton spin than $\phi_{ENS}^{\Gamma_2,neu}$ or $\phi_{ENS}^{J(0),neu}$ (see Figure 4).

To further investigate the relationship between the $\phi_{ENS}^{J(0),neu}$, $\phi_{ENS}^{six,neu}$, and $\phi_{ENS}^{\Gamma_1,neu}$ potentials and the electrostatic potential at a contact distance $U(R_C)$ based on Debye-Hückel theory (eq 32 in the Material and Method Section), we carried out simulations for the hard-sphere Coulombic potential model (Figure S10). In this model, $\phi_{ENS}^{six,neu}$ and $\phi_{ENS}^{\Gamma_1,neu}$ have almost superimposable profiles at a ^{1}H Larmor frequency of 900 MHz, and the values are much closer to $U(R_C)$ than to $\phi_{ENS}^{J(0),neu}$ (Figure S10A). The field dependence of $\phi_{ENS}^{\Gamma_1,neu}$ was also investigated using this theoretical model, and almost identical values of $\phi_{ENS}^{\Gamma_1,neu}$ are observed for ^{1}H Larmor frequencies ranging from 100 to 1000 MHz (Figure S10B).

In summary, we suggest that, for folded proteins, both the experimentally derived $\phi_{ENS}^{\Gamma_2,neu}$ and $\phi_{ENS}^{J(0),neu}$ potentials provide information that emphasizes long-range electrostatic interactions, possibly related to $\phi_{ENS,four}^{PB,neu}$, while the experimental $\phi_{ENS}^{six,neu}$ potential provides information that is pertinent to shorter-range electrostatic interactions that are proportional to $\phi_{ENS,six}^{PB,neu}$. Based on our analysis of $J(\omega)$ mentioned above (see Figure 4), we expect that the experimental $\phi_{ENS}^{\Gamma_1,neu}$ potential provides information on even shorter range electrostatic interactions than the $\phi_{ENS}^{six,neu}$ potential when sPREs are measured at high spectrometer fields. We also note that since the distance dependence of Γ_1 depends heavily on spectrometer field, with local information content (i.e., short-range interactions) becoming increasingly important at higher ^{1}H Larmor frequencies (see Figure 4), exactly how the experimental $\phi_{ENS}^{\Gamma_1,neu}$ potential relates to the Poisson-Boltzmann derived ϕ_{ENS} potentials still needs to be investigated by more rigorous analyses that are beyond the scope of the current work. We also note, however, that the $\phi_{ENS}^{\Gamma_1,neu}$ potential seems to depend only weakly on the ^{1}H frequency for our simple theoretical model. In the current study, we observe that the $\phi_{ENS}^{\Gamma_2,neu}$, $\phi_{ENS}^{J(0),neu}$, $\phi_{ENS}^{six,neu}$, and $\phi_{ENS}^{\Gamma_1,neu}$ potentials exhibit only minor differences in their profiles (Figure 8). We note, however that the difference between the maximum and minimum values of ϕ_{ENS} is larger for $\phi_{ENS}^{\Gamma_1,neu}$ than for $\phi_{ENS}^{six,neu}$ which in turn is larger than for $\phi_{ENS}^{J(0),neu}$. This is expected given the long-ranged nature of electrostatic interactions. For example, the $\phi_{ENS,six}^{PB,neu}$ and $\phi_{ENS,four}^{PB,neu}$ profiles are very similar for both ubiquitin (top panel of Figure 7A) and the unfolded state of drkN SH3 (bottom panel of Figure 7A).

A summary of the various sPRE-derived experimental and Poisson-Boltzmann theoretical forms of the ϕ_{ENS} potentials is provided in Table 1.

Validity of Poisson-Boltzmann Theory as a Basis for Evaluating Experimentally Derived ϕ_{ENS} Potentials. As noted by Yu et al.,[27−29,79] Poisson-Boltzmann theory is an approximate theory that treats the solvent as a continuum and does not necessarily provide an accurate description of ion distributions in and around the hydration shells of a protein. In particular, Poisson-Boltzmann theory does not explicitly take into account the role of solvent, and hence, the details of short-range electrostatic interactions, such as contact−ion pair and solvent-separated ion pair interactions,[27,80] are not distinguished. As a result, significantly different distributions of ions

https://doi.org/10.1021/jacs.2c10035
J. Am. Chem. Soc. 2022, 144, 21371−21388

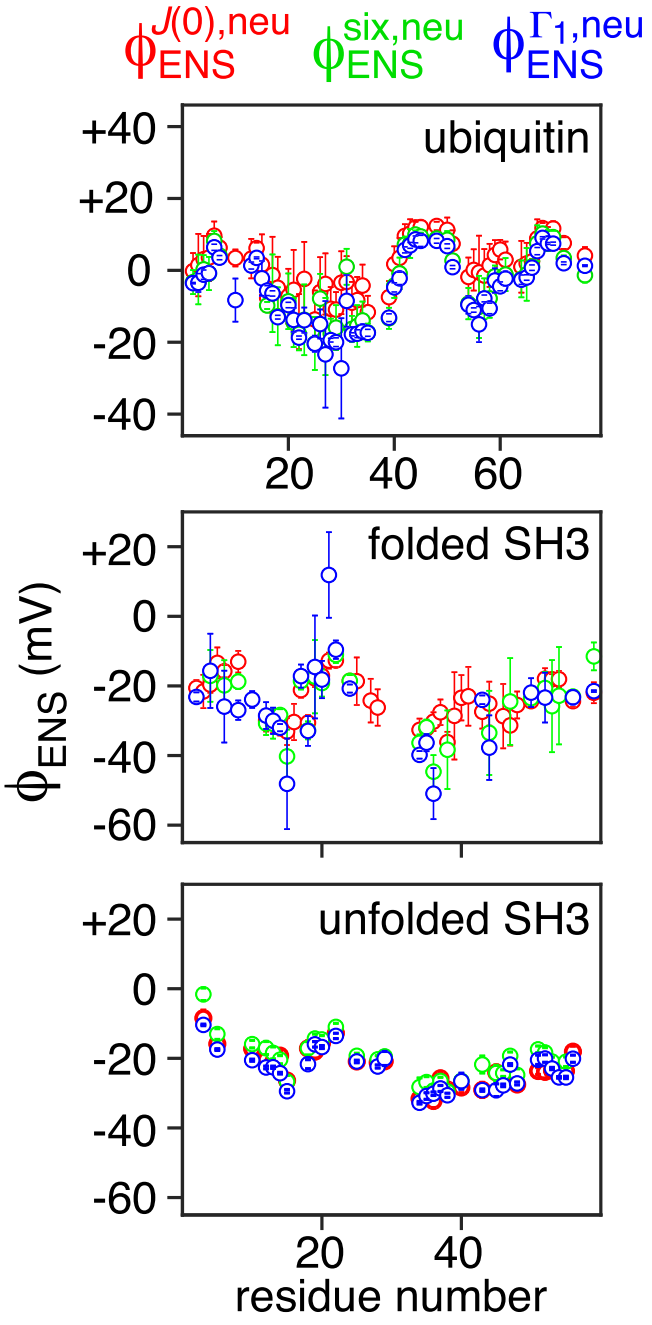

Figure 8. Comparisons between $\phi_{ENS}^{J(0),neu}$ (red), $\phi_{ENS}^{six,neu}$ (green), and $\phi_{ENS}^{\Gamma_1,neu}$ (blue) for ubiquitin and folded and unfolded drkN SH3. The Γ_1 data were measured at a spectrometer frequency of 500 MHz. Error bars represent 1 S.D.; rmsd, root mean square deviation.

around the protein hydration layer can be generated from Poisson-Boltzmann theory compared to theoretical models that make use of explicit solvent.[81]

Figure 9A shows why Poisson-Boltzmann theory can still provide a reasonably good estimate of the experimental ϕ_{ENS} potentials. The number and orientations of cosolutes that can be close to the protein surface are much smaller compared to those that are farther away due to the excluded volume effect (i.e., steric hindrance). As a result, cosolutes in the first and second hydration layers of the protein would contribute only a small amount to the sPRE and $\langle r^{-6}\rangle_{norm}$.

Table 1. Summary of Definitions of sPRE-derived Experimental and Poisson-Boltzmann Theoretical Electrostatic Near-Surface Potentials (ϕ_{ENS}) Used in the Current Work

sPRE-derived experimentally observable	
ϕ_{ENS}	$-\frac{k_BT}{2e}\ln\frac{\Gamma_2^{+ve}}{\Gamma_2^{-ve}}$
$\phi_{ENS}^{\Gamma_2,neu}$	$-\frac{k_BT}{e}\ln\frac{\Gamma_2^{neu}}{\Gamma_2^{-ve}}$
$\phi_{ENS}^{\Gamma_1,neu}$	$-\frac{k_BT}{e}\ln\frac{\Gamma_1^{neu}}{\Gamma_1^{-ve}}$
$\phi_{ENS}^{J(0),neu}$	$-\frac{k_BT}{e}\ln\frac{2\Gamma_2^{neu}-\Gamma_1^{neu}}{2\Gamma_2^{-ve}-\Gamma_1^{-ve}}$
$\phi_{ENS}^{six,neu}$	$-\frac{k_BT}{e}\ln\frac{\langle r^{-6}\rangle_{norm}^{neu}}{\langle r^{-6}\rangle_{norm}^{-ve}}$
Poisson-Boltzmann theoretical	
ϕ_{ENS}^{PB}	$-\frac{k_BT}{2e}\ln\frac{\int r^{-6}\exp\left(-\frac{\phi_{elec}^{+ve}(\vec{q})}{k_BT}\right)d\vec{q}}{\int r^{-6}\exp\left(-\frac{\phi_{elec}^{-ve}(\vec{q})}{k_BT}\right)d\vec{q}}$
$\phi_{ENS,six}^{PB,neu}$	$-\frac{k_BT}{e}\ln\frac{\int r^{-6}d\vec{q}}{\int r^{-6}\exp\left(-\frac{\phi_{elec}^{-ve}(\vec{q})}{k_BT}\right)d\vec{q}}$
$\phi_{ENS,four}^{PB,neu}$	$-\frac{k_BT}{e}\ln\frac{\int r^{-4}d\vec{q}}{\int r^{-4}\exp\left(-\frac{\phi_{elec}^{-ve}(\vec{q})}{k_BT}\right)d\vec{q}}$

A more quantitative analysis is afforded by examining the hypothetical radial distribution function $g(r)$ in the absence of any intermolecular interactions other than excluded volume, denoted as $g_{exc}(r)$. Figure 9B shows an example of the expected $g_{exc}(r)$ for the FFHS model (see Eqs S8.27−30), where it can be seen that $g(r)$ is negligibly small at short interspin separation (a few angstroms) and gradually increases to 1.

Similar trends are observed for a more realistic model based on the molecular coordinates of ubiquitin (see Materials and Methods Section). The $g(r)$ distribution functions for Lys29 of ubiquitin are shown in the left panels of Figure 9C. The top left panel of Figure 9C shows the various $g_{exc}(r)$ distribution functions calculated for 50 structures of ubiquitin (generated by refinement of the 10 solution NMR structures deposited in the protein data bank, PDB 1D3Z) (gray lines), with the mean $g_{exc}(r)$ in red. The top right panel shows the corresponding $g_{exc}(r)/r^4$ distribution function, which is the term that appears in eq 9: 4π times the area under the curve is equal to $\langle r^{-6}\rangle_{norm}^{exc}$. The right and left plots in the lower panels show the corresponding $g(r)$ and $g(r)/r^4$ distribution functions in the presence of Coulombic interactions based on Poisson-Boltzmann theory, denoted as $g_{PB}(r)$. Similar to the hard-sphere model, $g_{exc}(r)$ and $g_{PB}(r)$ start with very small values at short interspin separations and gradually increase at larger interspin separations. The $g(r)/r^4$ plot (Figure 9C, right panel) shows that the major contribution to $\langle r^{-6}\rangle_{norm}$ originates from cosolute molecules located between ∼5 and ∼15 Å from the proton spin. It should be noted, however, that these distributions can change significantly in the presence of short-range interactions, such as the hydrophobic effect and hydrogen bonding, which are neglected in these calculations. Our intention here is to demonstrate qualitatively that the

https://doi.org/10.1021/jacs.2c10035
J. Am. Chem. Soc. 2022, 144, 21371−21388

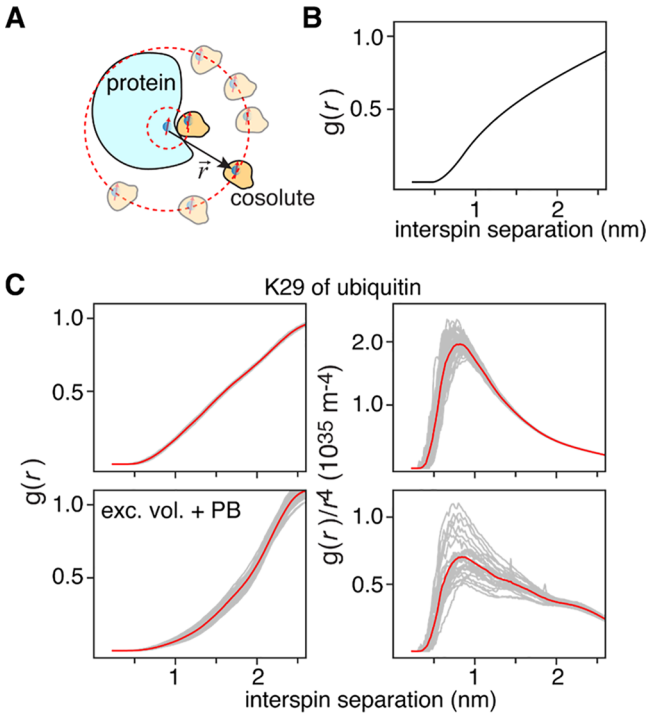

Figure 9. Distribution of the nitroxide cosolute around a protein. (A) Schematic of the distribution of the nitroxide cosolute around a protein. The red dashed line represents a circle at some fixed distance around a nuclear (^{1}H) spin of the protein. At small interspin separation between the protein proton and the cosolute electron spin, only a small number of cosolute molecules with restricted orientation can be accommodated. At large interspin separations, however, there are many cosolute molecules with unrestricted orientation. (B) Radial distribution function $g(r)$ expected for the Force-Free Hard-Sphere (FFHS) model calculated using eqs S8.26−S29, with parameters p = 11.6 Å, s = 2 Å, and R_C = 18.2 Å. (C) Radial distribution functions for Lys29 of ubiquitin (left panels): the hypothetical $g(r)$ with only excluded volume interaction is plotted in the left top panel, and $g(r)$ in the presence of an electrostatic potential given by the Poisson-Boltzmann theory (PB) is shown in the left bottom panel. 50 different conformers of ubiquitin were generated (see Material and Methods Section), and the corresponding $g(r)$ function is plotted in gray with the mean in red. The corresponding $g(r)/r^4$ distributions are shown in the right panels.

sPRE and $\langle r^{-6}\rangle_{norm}$ are not necessary determined by cosolutes located within <5 Å of the proton spin and that cosolutes located in the 5−15 Å range can make a dominant contribution.

We also observed some minor variations in $g_{exc}(r)$ and larger variations in $g_{PB}(r)$ among the ensemble of 50 refined ubiquitin structures, which are even more pronounced in the corresponding $g(r)/r^4$ plot (Figure 9C). The variations in $g_{PB}(r)$ are larger because the charge centers are located on surface sidechains (e.g., $N^{\zeta}H_3^+$ of lysine or carboxylate of glutamate) that are conformationally flexible even when the backbone is rigid (e.g. Lys29 of ubiquitin is located in the middle of an α-helix with a backbone order parameter squared of 0.89[82]) Therefore, it is important to take into account many different conformations of solvent-exposed sidechains to obtain accurate $\phi_{ENS,six}^{PB,neu}$ and $\phi_{ENS,four}^{PB,neu}$ values.

From our results, we suggest that any of the forms of the experimental ϕ_{ENS} potentials listed in Table 1 are not very sensitive to short-range interactions because of the small values of $g(r)$ at short interspin separations. As a result, the ϕ_{ENS} potentials can be calculated from Poisson-Boltzmann theory because cosolutes in the first or second hydration layer of the protein contribute minimally to the ϕ_{ENS} potential. This is particularly true for $\phi_{ENS}^{\Gamma_2,neu}$ and $\phi_{ENS}^{J(0),neu}$ as $J(0)$ and Γ_2 are long-ranged in nature (i.e., cosolutes at long distance from the nucleus of interest contribute a lot to $J(0)$). On the other hand, $\langle r^{-6}\rangle_{norm}$ and Γ_1 are more sensitive to short-range interactions. This may explain why the experimental $\phi_{ENS}^{six,neu}$ and $\phi_{ENS}^{\Gamma_1,neu}$ are systematically smaller than the theoretical $\phi_{ENS,six}^{PB,neu}$ ones (See Table S6), as the former are more sensitive to the short-range distribution of cosolute molecules around the proton of interest, and hence, a more accurate theoretical description near the protein surface would be required (e.g., inclusion of explicit solvent and hydrophobic interactions).

Effect of Short-Range Interactions on $\langle r^{-6}\rangle_{norm}$. The impact of short-range interactions between the nucleus of interest and the cosolute was investigated by placing two interaction sites on the nitroxide cosolute: one at the location of the unpaired electron on the cosolute (i.e., the paramagnetic center located on the oxygen atom) and the other at a site distant (the nitrogen atom of the carbamoyl group) from the paramagnetic center. In our model (see Materials and Methods Section), we included a square-well potential around either the oxygen atom of the nitroxide group (denoted as the O-model in Figure S11A) or the nitrogen atom of the carbamoyl group (denoted as the N-model in Figure S11B) of the 3-carbamoyl PROXYL cosolute. $\langle r^{-6}\rangle_{norm}^{exc}$ was set as the reference, that is, the model in the absence of any interactions other than the excluded volume (black line in Figures S11C,D). A significant increase in $\langle r^{-6}\rangle_{norm}$ is observed for the O-model (red lines in Figures S11C,D), whereas almost identical values were observed for the N-model (blue lines in Figures S11C,D), implying that interactions distant from the paramagnetic center do not significantly affect the value of $\langle r^{-6}\rangle_{norm}$. In the presence of electrostatic interactions, slightly different values of $\langle r^{-6}\rangle_{norm}$ are obtained (light blue lines in Figures S11C,D). For example, for drkN SH3, systematically lower values of $\langle r^{-6}\rangle_{norm}$ are observed relative to $\langle r^{-6}\rangle_{norm}^{exc}$, as the net charge on drkN SH3 is around −6 (and the negatively charged nitroxide cosolute has a charge of −1).

In summary, relative to $\langle r^{-6}\rangle_{norm}^{exc}$ computed solely from the excluded volume, a large effect on $\langle r^{-6}\rangle_{norm}$ is observed when the interaction site is located at the paramagnetic center of the nitroxide cosolute, but only a small effect is observed when the interaction site is distant from the paramagnetic center. This is particularly true when the protein−cosolute interaction is short-range in nature. If the interactions are long-range, however, such as Coulombic interactions, a significant change in $\langle r^{-6}\rangle_{norm}$ can occur even when the charge-center is distant from the paramagnetic center.

Concluding Remarks. In this paper, we focus on the sPRE from nitroxide-based cosolutes arising from outer-sphere relaxation. Outer-sphere relaxation results in distinct properties of the sPRE compared to those arising from inner-sphere relaxation. In particular, we show that the relative values of Γ_1 are heavily dependent on the spectrometer field and solvent viscosity for outer-sphere relaxation (e.g., for nitroxide-based radicals) but not for inner- or second-sphere relaxation mechanisms involving weak, rotationally correlated, protein−cosolute complexes. The relative values of Γ_2, on the other hand, are less dependent on spectrometer field or viscosity. Our theoretical model, based on the Smoluchowski diffusion

https://doi.org/10.1021/jacs.2c10035
J. Am. Chem. Soc. 2022, 144, 21371−21388

equation, shows that the spectral density $J(0)$ is linearly proportional to the inverse of the relative translational diffusion constant D_{trans}. Further, we uncover the possibility that $J(0)$ is related to $\langle r^{-4}\rangle_{norm}$ by eq 17, which holds up reasonably well for simple hard-sphere models in the presence of square-well or Coulomb potentials. Based on eq 17, a physical interpretation of the effective correlation time τ_C is afforded by eq 19, which produces the counterintuitive result that attractive intermolecular interactions actually lead to shorter τ_C values. The distance dependence of the spectral densities $J(0)$ and $J(\omega)$ at different spectrometer fields is also examined. Consistent with previous studies,[41,65] we find that the contribution of short-range interactions becomes significant for $J(\omega)$ at high fields, whereas long-range interactions dominate $J(0)$.

Various alternative methods, based on Γ_2, $J(0)$, Γ_1, and $\langle r^{-6}\rangle_{norm}$, for obtaining a quantitative description of the effective near-surface electrostatic potential (ϕ_{ENS}) for proteins from sPRE measurements are examined. We present four different experimentally derived potentials, $\phi_{ENS}^{\Gamma_2,neu}$, $\phi_{ENS}^{J(0),neu}$, $\phi_{ENS}^{\Gamma_1,neu}$, and $\phi_{ENS}^{six,neu}$ (see Table 1), and interpret these in terms of theoretical potentials based on Poisson-Boltzmann theory, $\phi_{ENS,six}^{PB,neu}$ and $\phi_{ENS,four}^{PB,neu}$, calculated directly from protein atomic coordinates. We show that each type of experimental ϕ_{ENS} potential provides different, distance-dependent information covering short-to long-range protein−cosolute interactions. Reasonably good agreement between the experimental $\phi_{ENS}^{\Gamma_2,neu}$ and theoretical $\phi_{ENS,six}^{PB,neu}$ potentials is observed for three different model protein systems: ubiquitin and the native and unfolded states of drkN SH3. An even better agreement between the experimental $\phi_{ENS}^{J(0),neu}$ and theoretical $\phi_{ENS,four}^{PB,neu}$ potentials is obtained for the two folded proteins (ubiquitin and the native state of drkN SH3), while for the unfolded state of drkN SH3, agreement of the experimental $\phi_{ENS}^{\Gamma_2,neu}$ potential with the theoretical $\phi_{ENS,six}^{PB,neu}$ and $\phi_{ENS,six}^{PB,neu}$ ones are broadly comparable (Figure 7). We suggest that this may be due to the fact that, for folded proteins, the molecular surface and hence the effective near-surface electrostatic potential only exhibit minor variations arising from surface side-chain conformational mobility, and consequently long-range interactions are the major contributor to the experimental $\phi_{ENS}^{J(0),neu}$ potential. The backbone for unfolded proteins, however, samples a very wide range of conformations in solution, such that contributions from longer range interactions may partially cancel out in the unfolded ensemble, while those from shorter range interactions show less variability as they involve individual residues or short stretches of neighboring residues in the amino acid sequence. As a consequence, the theoretical Poisson-Boltzmann $\phi_{ENS,four}^{PB,neu}$ potential, which is easily calculated for a folded protein, may be less accurate than the $\phi_{ENS,six}^{PB,neu}$ potential calculated from snapshots taken from a replica exchange molecular dynamics trajectory, owing to a degree of undersampling of the full unfolded conformational ensemble.

Finally, the orientation effect of the nitroxide cosolute was investigated. We found that $\langle r^{-6}\rangle_{norm}$ is sensitive to short-range interactions between the paramagnetic center on the cosolute (i.e., the location of the unpaired electron) and the nucleus of interest but becomes almost insensitive to short-range interactions when the interaction site on the cosolute is distant from the paramagnetic center. We also showed that $\langle r^{-6}\rangle_{norm}$ can be significantly influenced by long-range interactions (e.g., Coulombic) even when the interaction site on the cosolute is distant from the paramagnetic center.

MATERIALS AND METHODS

Experimental Data. All experimental sPRE data for ubiquitin[20] and the folded and unfolded states of drkN SH3[21] were taken from our previously published work. These data were acquired on Bruker 500, 800, or 900 MHz NMR spectrometers equipped with TCI z-axis gradient cryogenic probes. The sPRE data for ubiquitin were acquired at 298 K. For drkN SH3, we used sPRE data obtained at 277 K, where the exchange rate between the folded and unfolded states is negligibly small and can be neglected in the analysis of Γ_1 and Γ_2 rates.[21] The concentrations of ubiquitin and drkN SH3 were 500 and 200 μM, respectively. Both ubiquitin and drkN SH3 were dissolved in 10 mM phosphate buffer, pH 7.0, which corresponds to an ionic strength of 10 mM. The neutral and negatively charged nitroxide cosolutes employed in the current work were 3-(carbamoyl)-2,2,5,5-tetramethyl-1-pyrrolidinyloxy (3-carbamoyl PROXYL) and 3-(carboxy)-2,2,5,5-tetramethyl-1-pyrrolidinyloxy (3-carboxy PROXYL), respectively. The concentration of the nitroxide cosolutes was 25 mM for all NMR samples.

Model Potentials Used in the Hard Sphere Model. *Square-well potential model.* The square potential is given by

$$e^{-U(R)/k_BT} = \begin{cases} \alpha \text{ if } R_C \le R < R_b \\ 1 \text{ if } R_b \le R \end{cases} \quad (31)$$

where R is the center-to-center distance between protein and cosolute spheres; R_C is the contact distance between the protein and cosolute; and R_b is the well length. The well-depth of the square well potential is thus given by $-k_BT\ln(\alpha)$. R_b was set to R_C + 2 Å for all simulations in this study. The Force-Free Hard-Sphere model (FFHS)[54,55] corresponds to eq 31 with α = 1.

Coulomb potential model. Coulombic interactions in the presence of ions was approximated by the Debye-Hückel theory

$$U(R) = \frac{e^2 Z_s Z_p e^{\kappa R_C}}{4\pi\varepsilon_o\varepsilon_r(1+\kappa R_C)}\frac{e^{-\kappa R}}{R} \quad (32)$$

where the ionic strength is defined as $I = (1/2)\sum_j n_j Z_j^2$, and the square of the inverse of the Debye length as $\kappa^2 = 2I/(k_BT\varepsilon_o\varepsilon_r)$. Z_s and Z_p are the charge numbers on the cosolute and protein, respectively; e is the elementary charge; k_B is the Boltzmann constant; T is is the temperature; n_j is the number density of the j_{th} ion in solution (i.e., if c_j is the molar concentration of the j_{th} ion, then n_j = 1000 N_A c_j); N_A is Avogadro's number; ε_o is the vacuum permittivity; and ε_r is the relative permittivity (or dielectric constant). It should noted that many papers in the literature omit the factor of $4\pi\varepsilon_o$ in eq 32, and consequently, the equation corresponding to eq 32 may look different in these papers. Here we set ε_r equal to 78.5, which is approximately equal to the dielectric constant of water. The ionic strength was set to 0.01 M.

Calculation of the Radial Distribution Function from Protein Databank (PDB) Atomic Coordinates. Input PDB coordinates were rotated such that the bounding volume of the cubic box in Cartesian dimensions was minimized, thereby minimizing the number of grid points required in the calculation. These rotated coordinates were fed into the Adaptive Poisson-Boltzmann solver, APBS version 3.2.1 (http://apbs.readthedocs.io/en/stable/), which was instructed to generate a grid 25 Å larger than the bounds of the molecular coordinates on each side, with a spacing of 0.5 Å, and to output the electrostatic potential ϕ_i at each grid point i. Each grid point is associated with three cartesian coordinates, X_i, Y_i, Z_i, which specify the position to evaluate the electrostatic potential.

The abovementioned grid was also used for sampling cosolute configurations. At each grid point, the cosolute molecule (3-carbamoyl PROXYL or 3-carboxy PROXYL) was translated such that its centroid coincided with that point $\{X_i, Y_i, Z_i\}$, and given N_r = 50 pseudo-random rotations to uniformly sample the cosolute's

https://doi.org/10.1021/jacs.2c10035
J. Am. Chem. Soc. 2022, 144, 21371−21388

orientation, specified by the rotation axis $\hat{n}_j$ and rotation angle ψ_j. The uniformly random rotation was performed following the axis/angle formulation described in Section 17.10.1 of ref 83. The grid and orientation coordinates are collectively denoted as $\vec{q}_{ij} = \{X_i, Y_i, Z_i, \hat{n}_j, \psi_j\}$. $\vec{q}_{i,j}$ completely specifies the relative positions of the protein and the paramagnetic cosolute. Consequently, $\vec{q}_{i,j}$ determines the interspin separation between the paramagnetic center (O atom) on the nitroxide cosolute and the nucleus of interest in the protein.

The random rotation about the central grid point places the charge center, specified by $\vec{q}_{i,j}$, at a location where tricubic interpolation[84] was performed in three dimensions to evaluate the scalar field from values specified at the grid points. At the edges, the charge center may be outside of the grid, and this leads to extrapolation; that is spurious artifacts are expected the further one strays from the grid.

For each nucleus for which relaxation data was collected, the electrostatic-weighted distance distribution was computed as a histogram over the distance from the paramagnetic center to the nucleus in the range $r...r + \Delta r$, with contribution at distance r calculated as

$$g_n(r) = \sum_{\{i,j\} \in \Xi(r)} \eta r^{-2} \exp(-\phi(\vec{q}_{i,j})) \tag{33}$$

where n is the index for the nucleus of the interest. The normalization η is $\eta = \Delta x, \Delta y, \Delta z/(4\pi \Delta r \mathrm{N} r)$, where Δx, Δy, and Δz are the grid spacings in the three Cartesian dimensions. The summation was taken over the domain defined by:

$$\Xi(r') = \left\{ \{i,\ j\} | r' \le r(\vec{q}_{i,j}) \le r' + \Delta r \text{ and } \vec{q}_{i,j} \text{ does not clash} \right\} \tag{34}$$

The first condition of eq 34 specifies the coordinates $\vec{q}_{i,j}$, which gives the interspin distance $r(\vec{q}_{i,j})$ and also lies in $r \le r(\vec{q}_{ij}) \le r + \Delta r$. The second condition specifies the possible coordinate that the paramagnetic cosolute can occupy without steric clash with the protein. If there is no overlap between protein and cosolute atoms, the conformation is included in the distance distribution sums.

To simulate the effect of short-range interactions, a square-well potential of depth ε and length 4 Å was incorporated around the nucleus of interest. This modifies eq 33 to

$$g_n(r) = \sum_{\vec{q}_{i,j} \in \Xi(r)} \eta r^{-2} \alpha(\vec{q}_{i,j}) \exp(-\phi(\vec{q}_{i,j})) \tag{35}$$

where

$$\alpha(\vec{q}_{ij}) = \begin{cases} \varepsilon \text{ if } r(\vec{q}_{ij}) < 4\text{Å} \\ 1 \text{ else} \end{cases} \tag{36}$$

if the short-range interaction is placed between the O atom of the nitroxide moiety of the cosolute and the nucleus of interest; and

$$\alpha(\vec{q}_{ij}) = \begin{cases} \varepsilon \text{ if } r_{\mathrm{N}}(\vec{q}_{ij}) < 4\text{Å} \\ 1 \text{ else} \end{cases} \tag{37}$$

where r_{N} is the protein−carbamoyl nitrogen atom distance, if the short-range interaction is placed between the N atom of the carbamoyl group of the nitroxide cosolute and the nucleus of interest. The value of ε was set to 20, corresponding to a well-depth of $3k_{\mathrm{B}}T$.

For the unfolded state of drkN SH3, the calculation was performed over 100 snapshots from our previously published replica exchange molecular dynamics trajectory.[21] For the folded states of drkN SH3 and ubiquitin, 50 conformations were calculated by simulated annealing refinement of each of the 10 deposited structures in PDB entries 2A36[85] and 1D3Z,[86] respectively, under the influence of the deposited NMR restraints using the program Xplor-NIH.[87,88]

To optimize the representation of long-range electrostatics using APBS, we made use of a two-step calculation. The procedure described above was used to calculate the $g(r)$ distribution from 0 to 25 Å. To calculate the $g(r)$ distribution beyond 25 Å, a separate APBS calculation was performed using a grid 50 Å larger than the bounds of the molecular coordinates on each side, with a coarser spacing of 1.0 Å. Since cosolute molecules beyond 25 Å do not overlap with the protein of interest for any cosolute orientation and the distance from the actual location of the unpaired electron to the center of the cosolute is short compared to the distance between the cosolute and protein, the rotational contributions of the cosolute molecule to $g(r)$ can be safely ignored. Thus, for the second calculation, the cosolute was modeled as a sphere, with the unpaired electron placed at its center. This approximation increases the speed of the computation significantly. The radial distribution function from 25 to 50 Å, obtained from this second calculation, was then spliced together with the $g(r)$ obtained from 0 to 25 Å using the full atomic model for the cosolute to extend the $g(r)$ from 0 to 50 Å. $\langle r^{-6} \rangle_{\mathrm{norm}}$ and $\langle r^{-4} \rangle_{\mathrm{norm}}$ were calculated from $g(r)$ given by eq 33 or 35 followed by eq 9.

Units and Constants. $N_{\mathrm{A}} = 6.022 \times 10^{23}$ molecules; $\mu_{\mathrm{o}} = 4\pi \times 10^{-7}$ T^2·m^3·J^{-1}; $\hbar = 1.05 \times 10^{-34}$ J·s; $k_{\mathrm{B}} = 1.38 \times 10^{-23}$ J·K^{-1}; $\varepsilon_{\mathrm{o}} = 8.854 \times 10^{-12}$ C^2·J^{-1}·m^{-1}; $e = 1.602 \times 10^{-19}$ C; $\gamma_{\mathrm{H}} = 2.67 \times 10^8$ rad^{-1}·T^{-1}; and $\gamma_{\mathrm{e}} = 1.76 \times 10^{11}$ rad^{-1}·T^{-1}.

■ ASSOCIATED CONTENT

Supporting Information

The Supporting Information is available free of charge at https://pubs.acs.org/doi/10.1021/jacs.2c10035.

Discussion of inner-sphere versus outer-sphere relaxation mechanisms and their relative contribution to sPREs arising from nitroxide cosolutes based on an extensive dataset of ^{1}H relaxivity nuclear magnetic relaxation dispersion profiles and dynamic nuclear polarization coupling factors measured for DMSO, toluene, and acetone in the presence of TEMPOL; and derivations and mathematical underpinnings for the equations presented in the main text (PDF)

■ AUTHOR INFORMATION

Corresponding Author

G. Marius Clore − *Laboratory of Chemical Physics, National Institute of Diabetes and Digestive and Kidney Diseases, National Institutes of Health, Bethesda, Maryland 20892-0520, United States;* orcid.org/0000-0003-3809-1027; Email: mariusc@mail.nih.gov

Authors

Yusuke Okuno − *Laboratory of Chemical Physics, National Institute of Diabetes and Digestive and Kidney Diseases, National Institutes of Health, Bethesda, Maryland 20892-0520, United States*

Charles D. Schwieters − *Laboratory of Chemical Physics, National Institute of Diabetes and Digestive and Kidney Diseases, National Institutes of Health, Bethesda, Maryland 20892-0520, United States; Computational Biomolecular Magnetic Resonance Core, National Institute of Diabetes and Digestive and Kidney Diseases, National Institutes of Health, Bethesda, Maryland 20892-0520, United States*

Zhilin Yang − *Laboratory of Cell Biology, National Cancer Institute, National Institutes of Health, Bethesda, Maryland 20892, United States*

Complete contact information is available at: https://pubs.acs.org/10.1021/jacs.2c10035

Author Contributions

The manuscript was written through contributions of all the authors. All authors have given approval to the final version of the manuscript.

Notes

The authors declare no competing financial interest.

■ ACKNOWLEDGMENTS

We thank Drs. Attila Szabo, Irina Gopich, Robert Best, and Junji Iwahara for their helpful discussions and Drs. James Baber, Dan Garrett, and Jinfa Ying for technical support. This work was supported by the Intramural Program of the National Institute of Diabetes and Digestive and Kidney Diseases of the National Institutes of Health (to G.M.C.; Grant DK029023)

■ REFERENCES

(1) Petros, A. M.; Mueller, L.; Kopple, K. D. NMR Identification of Protein Surfaces Using Paramagnetic Probes. *Biochemistry* **1990**, *29*, 10041−10048.

(2) Fesik, S.; Gemmecker, G.; Olejniczak, E.; Petros, A. Identification of Solvent-Exposed Regions of Enzyme-Bound Ligands by Nuclear Magnetic Resonance. *J. Am. Chem. Soc.* **1991**, *113*, 7080−7081.

(3) Petros, A. M.; Neri, P.; Fesik, S. W. Identification of Solvent-Exposed Regions of an FK-506 Analog, Ascomycin, Bound to Fkbp Using a Paramagnetic Probe. *J. Biomol. NMR* **1992**, *2*, 11−18.

(4) Esposito, G.; Lesk, A. M.; Molinari, H.; Motta, A.; Niccolai, N.; Pastore, A. Probing Protein Structure by Solvent Perturbation of Nuclear Magnetic Resonance Spectra: Nuclear Magnetic Resonance Spectral Editing and Topological Mapping in Proteins by Paramagnetic Relaxation Filtering. *J. Mol. Biol.* **1992**, *224*, 659−670.

(5) Moore, C. D.; Lecomte, J. T. Characterization of an Independent Structural Unit in Apocytochrome B5. *Biochemistry* **1993**, *32*, 199−207.

(6) Improta, S.; Molinari, H.; Pastore, A.; Consonni, R.; Zetta, L. Probing Protein Structure by Solvent Perturbation of NMR Spectra: A Comparison with Photochemically Induced Dynamic Nuclear Polarization Techniques Applied to Native α-Lactalbumin. *Eur. J. Biochem.* **1995**, *227*, 78−86.

(7) Improta, S.; Molinari, H.; Pastore, A.; Consonni, R.; Zetta, L. Probing Protein Structure by Solvent Perturbation of NMR Spectra. Photochemically Induced Dynamic Nuclear Polarization and Paramagnetic Perturbation Techniques Applied to the Study of the Molten Globule State of α-Lactalbumin. *Eur. J. Biochem.* **1995**, *227*, 87−96.

(8) Molinari, H.; Esposito, G.; Ragona, L.; Pegna, M.; Niccolai, N.; Brunne, R. M.; Lesk, A. M.; Zetta, L. Probing Protein Structure by Solvent Perturbation of NMR Spectra: The Surface Accessibility of Bovine Pancreatic Trypsin Inhibitor. *Biophys. J.* **1997**, *73*, 382−396.

(9) Scarselli, M.; Bernini, A.; Segoni, C.; Molinari, H.; Esposito, G.; Lesk, A. M.; Laschi, F.; Temussi, P.; Niccolai, N. Tendamistat Surface Accessibility to the TEMPOL Paramagnetic Probe. *J. Biomol. NMR* **1999**, *15*, 125−133.

(10) Niccolai, N.; Ciutti, A.; Spiga, O.; Scarselli, M.; Bernini, A.; Bracci, L.; Di Maro, D.; Dalvit, C.; Molinari, H.; Esposito, G.; Temussi, P. A. NMR Studies of Protein Surface Accessibility. *J. Biol. Chem.* **2001**, *276*, 42455−42461.

(11) Niccolai, N.; Spadaccini, R.; Scarselli, M.; Bernini, A.; Crescenzi, O.; Spiga, O.; Ciutti, A.; Di Maro, D.; Bracci, L.; Dalvit, C.; Temussi, P. A. Probing the Surface of a Sweet Protein: NMR Study of Mnei with a Paramagnetic Probe. *Protein Sci.* **2001**, *10*, 1498−1507.

(12) Pintacuda, G.; Otting, G. Identification of Protein Surfaces by NMR Measurements with a Paramagnetic Gd(III) Chelate. *J. Am. Chem. Soc.* **2002**, *124*, 372−373.

(13) Hernández, G.; Teng, C.-L.; Bryant, R. G.; LeMaster, D. M. O2 Penetration and Proton Burial Depth in Proteins: Applicability to Fold Family Recognition. *J. Am. Chem. Soc.* **2002**, *124*, 4463−4472.

(14) Niccolai, N.; Spiga, O.; Bernini, A.; Scarselli, M.; Ciutti, A.; Fiaschi, I.; Chiellini, S.; Molinari, H.; Temussi, P. A. NMR Studies of Protein Hydration and Tempol Accessibility. *J. Mol. Biol.* **2003**, *332*, 437−447.

(15) Bernini, A.; Venditti, V.; Spiga, O.; Ciutti, A.; Prischi, F.; Consonni, R.; Zetta, L.; Arosio, I.; Fusi, P.; Guagliardi, A.; Niccolai, N. NMR Studies on the Surface Accessibility of the Archaeal Protein Sso7d by Using Tempol and Gd (III)(DTPA-BMA) as Paramagnetic Probes. *Biophys. Chem.* **2008**, *137*, 71−75.

(16) Bernini, A.; Venditti, V.; Spiga, O.; Niccolai, N. Probing Protein Surface Accessibility with Solvent and Paramagnetic Molecules. *Progr. Nucl. Magn. Reson. Spec.* **2009**, *54*, 278−289.

(17) Madl, T.; Güttler, T.; Görlich, D.; Sattler, M. Structural Analysis of Large Protein Complexes Using Solvent Paramagnetic Relaxation Enhancements. *Angewandte Chemie Int. Ed.* **2011**, *50*, 3993−3997.

(18) Kosol, S.; Contreras-Martos, S.; Cedeño, C.; Tompa, P. Structural Characterization of Intrinsically Disordered Proteins by NMR Spectroscopy. *Molecules* **2013**, *18*, 10802−10828.

(19) Gong, Z.; Schwieters, C. D.; Tang, C. Theory and Practice of Using Solvent Paramagnetic Relaxation Enhancement to Characterize Protein Conformational Dynamics. *Methods* **2018**, *148*, 48−56.

(20) Okuno, Y.; Szabo, A.; Clore, G. M. Quantitative Interpretation of Solvent Paramagnetic Relaxation for Probing Protein−Cosolute Interactions. *J. Am. Chem. Soc.* **2020**, *142*, 8281−8290.

(21) Okuno, Y.; Yoo, J.; Schwieters, C. D.; Best, R. B.; Chung, H. S.; Clore, G. M. Atomic View of Cosolute-Induced Protein Denaturation Probed by NMR Solvent Paramagnetic Relaxation Enhancement. *Proc. Natl. Acad. Sci. U.S.A.* **2021**, *118*, No. e211202118.

(22) McLaughlin, A.; Grathwohl, C.; McLaughlin, S. The Adsorption of Divalent Cations to Phosphatidylcholine Bilayer Membranes. *Biochim. Biophys. Acta − Biomembranes* **1978**, *513*, 338−357.

(23) MCLaughlin, A.; Grathwohl, C.; Richards, R. The Interaction of Cobalt with Glycerophosphoryl Choline and Phosphatidyl Choline Bilayer Membranes. *J. Magn. Reson.* **1978**, *31*, 283−293.

(24) Lau, A.; McLaughlin, A.; McLaughlin, S. The Adsorption of Divalent Cations to Phosphatidylglycerol Bilayer Membranes. *Biochim. Biophys. Acta -− Biomembranes* **1981**, *645*, 279−292.

(25) Cafiso, D.; McLaughlin, A.; McLaughlin, S.; Winiski, A. Measuring Electrostatic Potentials Adjacent to Membranes. *Meth. Enymol.* **1989**, *171*, 342−364.

(26) Likhtenshtein, G. I.; Adin, I.; Novoselsky, A.; Shames, A.; Vaisbuch, I.; Glaser, R. NMR Studies of Electrostatic Potential Distribution around Biologically Important Molecules. *Biophys. J.* **1999**, *77*, 443−453.

(27) Yu, B.; Iwahara, J. Experimental Approaches for Investigating Ion Atmospheres around Nucleic Acids and Proteins. *Comp. Struct. Biotech. J.* **2021**, *19*, 2279−2285.

(28) Yu, B.; Pletka, C. C.; Pettitt, B. M.; Iwahara, J. De Novo Determination of near-Surface Electrostatic Potentials by NMR. *Proc. NAtl. Acad. Sci. U.S.A.* **2021**, *118*, No. e2104020118.

(29) Yu, B.; Pletka, C. C.; Iwahara, J. Protein Electrostatics Investigated through Paramagnetic Nmr for Nonpolar Groups. *J. Phys. Chem. B* **2022**, *126*, 2196−2202.

(30) Peters, J.; Huskens, J.; Raber, D. Lanthanide Induced Shifts and Relaxation Rate Enhancements. *Prog. Nucl. Magn. Reson. Spec.* **1996**, *28*, 283−350.

(31) Vigouroux, C.; Bardet, M.; Belorizky, E.; Fries, P.; Guillermo, A. Nuclear and Electronic Relaxation in Lanthanide Solutions:$(CH_3)4N^+/Gd^{3+}$ Repulsive Ion Pair in D_2O. *Chem. Phys. Lett.* **1998**, *286*, 93−100.

(32) Chen, J.; Belford, R.; Clarkson, R. Second-Sphere and Outer-Sphere Proton Relaxation of Paramagnetic Complexes: From EPR to NMRD. *J. Phys. Chem. A* **1998**, *102*, 2117−2130.

https://doi.org/10.1021/jacs.2c10035
J. Am. Chem. Soc. 2022, 144, 21371−21388

(33) Botta, M. Second Coordination Sphere Water Molecules and Relaxivity of Gadolinium (III) Complexes: Implications for MRI Contrast Agents. *Eur. J. Inorg. Chem.* **2000**, *2000*, 399−407.
(34) Aime, S.; Botta, M.; Terreno, E. Gd (III)-Based Contrast Agents for Mri. *Adv. Inorg. Chem.* **2005**, *57*, 173−237.
(35) Hocking, H. G.; Zangger, K.; Madl, T. *Solution Pre Nmr*. In *Protein Nmr*; Berliner, L., Ed.; Springer: Boston MA, 2015, pp 133−157. DOI: 10.1007/978-1-4899-7621-5_4
(36) Sezer, D.; Prandolini, M.; Prisner, T. F. Dynamic Nuclear Polarization Coupling Factors Calculated from Molecular Dynamics Simulations of a Nitroxide Radical in Water. *Phys. Chem. Chem. Phys.* **2009**, *11*, 6626−6637.
(37) Neugebauer, P.; Krummenacker, J. G.; Denysenkov, V. P.; Parigi, G.; Luchinat, C.; Prisner, T. F. Liquid State Dnp of Water at 9.2 T: An Experimental Access to Saturation. *Phys. Chem. Chem. Phys.* **2013**, *15*, 6049−6056.
(38) Neugebauer, P.; Krummenacker, J. G.; Denysenkov, V. P.; Helmling, C.; Luchinat, C.; Parigi, G.; Prisner, T. F. High-Field Liquid State NMR Hyperpolarization: A Combined DNP/NMRD Approach. *Phys. Chem. Chem. Phys.* **2014**, *16*, 18781−18787.
(39) Sezer, D. Rationalizing Overhauser DNP of Nitroxide Radicals in Water through MD Simulations. *Phys. Chem. Chem. Phys.* **2014**, *16*, 1022−1032.
(40) Toyama, Y.; Rangadurai, A. K.; Forman-Kay, J. D.; Kay, L. E. Mapping the Per-Residue Surface Electrostatic Potential of Caprin1 Along Its Phase-Separation Trajectory. *Proc. Natl. Acad. Sci. U.S.A.* **2022**, *119*, No. e2210492119.
(41) Halle, B. Cross-Relaxation between Macromolecular and Solvent Spins: The Role of Long-Range Dipole Couplings. *J. Chem. Phys.* **2003**, *119*, 12372−12385.
(42) Hubbard, P. S. Some Properties of Correlation Functions of Irreducible Tensor Operators. *Phys. Rev.* **1969**, *180*, 319.
(43) Clore, G. M.; Iwahara, J. Theory, Practice, and Applications of Paramagnetic Relaxation Enhancement for the Characterization of Transient Low-Population States of Biological Macromolecules and Their Complexes. *Chem. Rev.* **2009**, *109*, 4108−4139.
(44) Abragam, P. A.; Abragam, A. *The Principles of Nuclear Magnetism*; Clarendon Press, 1961.
(45) Guéron, M. Nuclear Relaxation in Macromolecules by Paramagnetic Ions: A Novel Mechanism. *J. Magn. Reson.* **1975**, *19*, 58−66.
(46) Cavanagh, J.; Fairbrother, W. J.; Palmer, A. G., III; Skelton, N. J., *Protein NMR Spectroscopy: Principles and Practice*. 2nd ed.; Elsevier: San Diego CA, 1995.
(47) Kulikov, A.; Likhtenstein, G. The Use of Spin Relaxation Phenomena in the Investigation of the Structure of Model and Biological Systems by the Method of Spin Labels. *Advances in molecular relaxation and interaction processes* **1977**, *10*, 47−79.
(48) Schwartz, L. J.; Stillman, A. E.; Freed, J. H. Analysis of Electron Spin Echoes by Spectral Representation of the Stochastic Liouville Equation. *J. Chem. Phys.* **1982**, *77*, 5410−5425.
(49) Kuzhelev, A. A.; Strizhakov, R. K.; Krumkacheva, O. A.; Polienko, Y. F.; Morozov, D. A.; Shevelev, G. Y.; Pyshnyi, D. V.; Kirilyuk, I. A.; Fedin, M. V.; Bagryanskaya, E. G. Room-Temperature Electron Spin Relaxation of Nitroxides Immobilized in Trehalose: Effect of Substituents Adjacent to No-Group. *J. Magn. Reson.* **2016**, *266*, 1−7.
(50) Fries, P. H. Model-Free Nuclear Magnetic Resonance Study of Intermolecular Free Energy Landscapes in Liquids with Paramagnetic Ln^{3+} Spotlights: Theory and Application to Arg-Gly-Asp. *J. Chem. Phys.* **2012**, *136*, 01B614.
(51) Caravan, P. Strategies for Increasing the Sensitivity of Gadolinium Based MRI Contrast Agents. *Chem. Soc. Rev.* **2006**, *35*, 512−523.
(52) Solomon, I. Relaxation Processes in a System of Two Spins. *Phys. Rev.* **1955**, *99*, 559.
(53) Bloembergen, N.; Morgan, L. Proton Relaxation Times in Paramagnetic Solutions. Effects of Electron Spin Relaxation. *J. Chem. Phys.* **1961**, *34*, 842−850.
(54) Hwang, L. P.; Freed, J. H. Dynamic Effects of Pair Correlation Functions on Spin Relaxation by Translational Diffusion in Liquids. *J. Chem. Phys.* **1975**, *63*, 4017−4025.
(55) Ayant, Y.; Belorizky, E.; Aluzon, J.; Gallice, J. Calculation of Spectral Densities for Relaxation Resulting from Random Molecular Translational Modulation of Magnetic Dipolar Coupling in Liquids. *J. Physique* **1975**, *36*, 991−1004.
(56) Bennati, M.; Luchinat, C.; Parigi, G.; Türke, M.-T. Water ^{1}H Relaxation Dispersion Analysis on a Nitroxide Radical Provides Information on the Maximal Signal Enhancement in Overhauser Dynamic Nuclear Polarization Experiments. *Phys. Chem. Chem. Phys.* **2010**, *12*, 5902−5910.
(57) Hodges, M. W.; Cafiso, D. S.; Polnaszek, C. F.; Lester, C. C.; Bryant, R. G. Water Translational Motion at the Bilayer Interface: An NMR Relaxation Dispersion Measurement. *Biophys. J.* **1997**, *73*, 2575−2579.
(58) Polnaszek, C.; Bryant, R. Nitroxide Radical Induced Solvent Proton Relaxation: Measurement of Localized Translational Diffusion. *J. Chem. Phys.* **1984**, *81*, 4038−4045.
(59) Armstrong, B. D.; Han, S. Overhauser Dynamic Nuclear Polarization to Study Local Water Dynamics. *J. Am. Chem. Soc.* **2009**, *131*, 4641−4647.
(60) Höfer, P.; Parigi, G.; Luchinat, C.; Carl, P.; Guthausen, G.; Reese, M.; Carlomagno, T.; Griesinger, C.; Bennati, M. Field Dependent Dynamic Nuclear Polarization with Radicals in Aqueous Solution. *J. Am. Chem. Soc.* **2008**, *130*, 3254−5.
(61) Frezzato, D.; Rastrelli, F.; Bagno, A. Nuclear Spin Relaxation Driven by Intermolecular Dipolar Interactions: The Role of Solute−Solvent Pair Correlations in the Modeling of Spectral Density Functions. *J. Phys. Chem. B* **2006**, *110*, 5676−5689.
(62) Fries, P. H.; Imbert, D.; Melchior, A. Determination of Outer-Sphere Dipolar Time Correlation Functions from High-Field Nmr Measurements. Example of a Gd^{3+} Complex in a Viscous Solvent. *J. Chem. Phys.* **2010**, *132*, 044502.
(63) Zhang, O.; Forman-Kay, J. D. Structural Characterization of Folded and Unfolded States of an SH3 Domain in Equilibrium in Aqueous Buffer. *Biochemistry* **1995**, *34*, 6784−6794.
(64) Küçük, S. E.; Neugebauer, P.; Prisner, T. F.; Sezer, D. Molecular Simulations for Dynamic Nuclear Polarization in Liquids: A Case Study of TEMPOL in Acetone and DMSO. *Phys. Chem. Chem. Phys.* **2015**, *17*, 6618−28.
(65) Gabl, S.; Steinhauser, O.; Weingärtner, H. From Short-Range to Long-Range Intermolecular Noes in Ionic Liquids: Frequency Does Matter. *Angewandte Chemie Int. Ed.* **2013**, *52*, 9242−9246.
(66) McConnell, H. M. Reaction Rates by Nuclear Magnetic Resonance. *J. Chem. Phys.* **1958**, *28*, 430−431.
(67) Swift, T. J.; Connick, R. E. Nmr-Relaxation Mechanisms of O^{17} in Aqueous Solutions of Paramagnetic Cations and the Lifetime of Water Molecules in the First Coordination Sphere. *J. Chem. Phys.* **1962**, *37*, 307−320.
(68) Luz, Z.; Meiboom, S. Proton Relaxation in Dilute Solutions of Cobalt (II) and Nickel (II) Ions in Methanol and the Rate of Methanol Exchange of the Solvation Sphere. *J. Chem. Phys.* **1964**, *40*, 2686−2692.
(69) Lester, C. C.; Bryant, R. G. *Paramagnetic Relaxation of Water Protons Effects of Nonbonded Interactions, Electron Spin Relaxation, and Rotational Immobilization* Berliner, L. J., Reuben, J., Eds.; Plenum Press: New York, 1993; Vol. *12*, pp 113−132.*NMR of Paramagnetic Molecules* DOI: 10.1007/978-1-4615-2886-9_3
(70) Kowalewski, J.; Nordenskiöld, L.; Benetis, N.; Westlund, P.-O. Theory of Nuclear Spin Relaxation in Paramagnetic Systems in Solution. *Progr. Nucl. Magn. Reson. Spec.* **1985**, *17*, 141−185.
(71) Bryant, R. G. The Dynamics of Water-Protein Interactions. *nn. Rev. Biophys. Biomol. Struct.* **1996**, *25*, 29−53.
(72) Eletsky, A.; Moreira, O.; Kovacs, H.; Pervushin, K. A Novel Strategy for the Assignment of Side-Chain Resonances in Completely Deuterated Large Proteins Using ^{13}C Spectroscopy. *J. Biomol. NMR* **2003**, *26*, 167−179.

(73) Teng, C.-L.; Bryant, R. G. Spin Relaxation Measurements of Electrostatic Bias in Intermolecular Exploration. *J. Magn. Reson.* **2006**, *179*, 199−205.
(74) Glaser, R.; Novoselsky, A.; Shames, A.; Likhtenshtein, G. I. NMR Studies of Electrostatic Fields around Charged Monosaccharides and Related Molecules. *Israel J. Chem.* **2000**, *40*, 263−269.
(75) Leniart, D. S.; Connor, H. D.; Freed, J. H. An ESR and ENDOR Study of Spin Relaxation of Semiquinones in Liquid Solution. *J. Chem. Phys.* **1975**, *63*, 165−199.
(76) Honig, B.; Nicholls, A. Classical Electrostatics in Biology and Chemistry. *Science* **1995**, *268*, 1144−1149.
(77) Fogolari, F.; Brigo, A.; Molinari, H. The Poisson−Boltzmann Equation for Biomolecular Electrostatics: A Tool for Structural Biology. *J. Mol. Recogn.* **2002**, *15*, 377−392.
(78) Evans, D. The Determination of the Paramagnetic Susceptibility of Substances in Solution by Nuclear Magnetic Resonance. *J. Chem. Soc.* **1959**, 2003−2005.
(79) Yu, B.; Pettitt, B. M.; Iwahara, J. Dynamics of Ionic Interactions at Protein−Nucleic Acid Interfaces. *Acc. Chem. Res.* **2020**, *53*, 1802−1810.
(80) Chen, C.; Esadze, A.; Zandarashvili, L.; Nguyen, D.; Pettitt, B. M.; Iwahara, J. Dynamic Equilibria of Short-Range Electrostatic Interactions at Molecular Interfaces of Protein−DNA Complexes. *J. Phys. Chem. Lett.* **2015**, *6*, 2733−2737.
(81) Giambaşu, G. M.; Luchko, T.; Herschlag, D.; York, D. M.; Case, D. A. Ion Counting from Explicit-Solvent Simulations and 3D-RISM. *Biophys. J.* **2014**, *106*, 883−94.
(82) Tjandra, N.; Szabo, A.; Bax, A. Protein Backbone Dynamics and ^{15}N Chemical Shift Anisotropy from Quantitative Measurement of Relaxation Interference Effects. *J. Am. Chem. Soc.* **1996**, *118*, 6986−6991.
(83) Brannon, R. *Rotation, Reflection, and Frame Changes*. In *Orthogonal Tensors in Computational Engineering Mechanics*; IOP Publishing: Bristol, 2018.
(84) Lekien, F.; Marsden, J. Tricubic Interpolation in Three Dimensions. *Int. J. Num. Meth. Eng.* **2005**, *63*, 455−471.
(85) Bezsonova, I.; Singer, A.; Choy, W. Y.; Tollinger, M.; Forman-Kay, J. D. Structural Comparison of the Unstable DrnK SH3 Domain and a Stable Mutant. *Biochemistry* **2005**, *44*, 15550−15560.
(86) Cornilescu, G.; Marquardt, J. L.; Ottiger, M.; Bax, A. Validation of Protein Structure from Anisotropic Carbonyl Chemical Shifts in Dilute Liquid Crystalline Phase. *J. Am. Chem. Soc.* **1998**, *120*, 6836−6837.
(87) Schwieters, C. D.; Kuszewski, J. J.; Tjandra, N.; Marius Clore, G. M. The Xplor-NIH NMR Molecular Structure Determination Package. *J. Magn. Reson.* **2003**, *160*, 65−73.
(88) Schwieters, C. D.; Bermejo, G. A.; Clore, G. M. Xplor-NIH for Molecular Structure Determination from NMR and Other Data Sources. *Protein Sci.* **2018**, *27*, 26−40.

https://doi.org/10.1021/jacs.2c10035
J. Am. Chem. Soc. 2022, 144, 21371−21388